

STRATEGIES FOR COMPUTING THE SCALAR SELF-FORCE ON A  
SCHWARZSCHILD BACKGROUND: A COMPARISON STUDY WITH AN FORTRAN  
CODE IN C++, EXTRAPOLATING TO INFINITE DISCONTINUOUS GALERKIN  
ORDER, AND EXTRAPOLATING TO INFINITE SPHERICAL HARMONIC MODES

A Thesis/Dissertation

Submitted to the Graduate Faculty of the  
Louisiana State University and  
Agricultural and Mechanical College  
in partial fulfillment of the  
requirements for the degree of  
Master of Science

in

Physics

by

Steven (Susan) Dorsher

B.S., Massachusetts Institute of Technology, 2004

M.S., The Ohio State University, 2006

M.S., University of Minnesota, 2013

December, 2017

# Acknowledgments

I would like to thank Peter Diener and Frank Löffler for their guidance. Peter Diener especially has been very important to me, both as an advisor and personally. I would also like to thank Gabriela Gonzalez for the excellent opportunity to work on LIGO during the time of three detections, which provided me the funding I needed to continue the work detailed in this document. I would like to thank Juana Moreno for the opportunity to work as outreach coordinator to the LA-SIGMA Research Experience for Undergraduates program my first summer at LSU, which also helped provide funding for this research. My parents, Paul and Joanne Dorsher, also deserve a mention, both for extraordinary moral support and for the financial support they provided that helped make this possible. I would also like to thank my sister, Patricia Dorsher, and my friends Christy Paulson, Hope Ring, Steve Brandt, Brad Schaefer, Luke, and Josh McKeown.

# Table of Contents

ACKNOWLEDGMENTS .....	ii
LIST OF TABLES .....	v
LIST OF FIGURES .....	vi
ABSTRACT .....	xi
CHAPTER	
1 INTRODUCTION .....	1
1.1 Gravitational Waves .....	1
1.2 Extreme Mass Ratio Inspirals .....	2
1.3 EMRIs .....	2
1.4 The discontinuous galerkin method .....	2
1.5 LISA .....	2
2 A SIMPLE NUMERICAL SOLUTION FOR A PDE USING THE DISCONTINUOUS GALERKIN METHOD .....	3
2.1 Reduction to coupled first order differential equations .....	3
2.2 Spatial grids .....	4
2.2.1 Finite difference schemes .....	4
2.2.2 The Disctontinuous Galerkin method .....	5
2.3 Time evolution .....	7
2.4 Wave equation on flat spacetime .....	7
3 A SCALAR FIELD ON A SCHWARZSCHILD BACKGROUND WITHOUT A SOURCE .....	11
3.1 Scalar field on Schwarzschild spacetime .....	11
3.1.1 Multipole moment decomposition .....	11
3.1.2 Hyperboloidal compactification .....	11
3.1.3 Initial conditions .....	11
3.1.4 final results .....	11
4 CIRCULAR ORBITS ON A SCHWARZSCHILD SPACETIME .....	16
4.1 $\phi$ of $t$ .....	16
4.1.1 Effective source .....	16
4.1.2 World tube .....	16
4.1.3 Comparison between C++ and Fortran codes .....	16
5 ELLIPTICAL ORBITS ON A SCHWARZSCHILD SPACETIME .....	20
5.0.1 Time dependent coordinate transformation .....	20
5.0.2 orbital parameters (osculating orbits paper) .....	20

6	EXTRAPOLATING THE SELF FORCE TO INFINITE DISCONTINUOUS GALERKIN ORDER .....	25
6.0.1	Checking for discontinuities in $F_{\text{inf}}$ for each each l-mode .....	25
6.0.2	Determining $F_{\text{inf}}$ using maximum likelihood fits to subsegments of lines in semilog space .....	26
7	EXTRAPOLATING THE MODE-SUMMED SELF-FORCE TO INCLUDE CONTRIBUTIONS FROM AN INFINITE NUMBER OF SPHERICAL HARMONIC MODES.....	35
7.0.1	Fractional errors.....	37
7.0.2	Structure of the error compared to the evolu- tion in time .....	37
8	IMPROVING MODE FITS VIA A POWER LAW SCALED WEIGHT FACTOR IN $\chi^2$ SUM .....	45
8.0.1	Relative error as a function of mode .....	45
8.1	ToDO .....	45
9	FUTURE WORK: GENERIC ORBITS VIA THE OSCU- LATING ORBITS FRAMEWORK.....	49
9.1	plans for the future .....	49
9.1.1	methods .....	49
	REFERENCES.....	50
	VITA .....	54

# List of Tables

6.1	Manual starting indices and $F_{\text{inf}}$ values for $t=632$ , $l=2$ . . . . .	25
-----	---	----

# List of Figures

2.1	Waves evolving over time for gaussian initial conditions .....	8
2.2	Waves evolving over time for sinusoidal initial conditions .....	8
2.3	$L_2$ error scaling with DG order for sinusoidal initial conditions .....	9
2.4	$L_2$ error scaling with element size for sinusoidal initial conditions .....	10
3.1	Quasinormal mode for $l=1, m=1$ .....	12
3.2	Quasinormal mode for $l=2, m=2$ .....	12
3.3	Power law tail, $l=1, m=1$ .....	13
3.4	Power law tail does not match expectations due to truncation error in DG method, $l=2, m=2$ .....	13
3.5	Scalar field spatial slice initial condition and first full timestep for $l=0$ . .....	14
3.6	Time derivative of the scalar field spatial slice initial condition and first full timestep for $l=0$ . .....	14
3.7	Radial derivative of the scalar field spatial slice initial condition and first full timestep for $l=0$ . .....	15
4.1	Spatial slice of the world tube window function. ....	17
4.2	Add or subtract the singular field to either side of the world tube boundary before performing the time dependent coordinate transform (or inverting it) to obtain the retarded field in the exterior region and the regularized field in the interior region. ....	17
4.3	Comparison between Fortran and C++ codes for a particle on a circular orbit, $l=0, m=0$ . ....	18
4.4	Comparison between Fortran and C++ codes for a particle on a circular orbit, $l=1, m=1$ . ....	18
4.5	Comparison between Fortran and C++ codes for a particle on a circular orbit, $l=2, m=0$ . ....	19
4.6	Comparison between Fortran and C++ codes for a particle on a circular orbit, $l=2, m=2$ . ....	19

5.1	Schwarzschild $r$ as a function of time over several orbits.....	21
5.2	Plotting $\chi$ as the angle in polar coordinates, the orbit forms an exact ellipse. This is the definition of $\chi$ , provided $r$ is in Schwarzschild coordinates. Shown for $p = 9.9$ and $e = 0.1$ , DG order 44.....	21
5.3	Plotting the orbit as it physically would exist, using Schwarzschild $\phi$ as the polar coordinate angle, the orbit precesses but does not inspiral since there is no generic evolution yet. Shown for $p = 9.9$ and $e = 0.1$ , DG order 44.....	22
5.4	Precession of the elliptical orbit is demonstrated due to the inequality in the period of the angular variables $\chi$ , which represents the period of the radial oscillations, and $\phi$ , which represents the period of the angular oscillations. $p = 9.9$ , $e = 0.1$ , DG order 44.....	22
5.5	Raw output of Diener, Warburton, and Wardell code for DG order 44. Radial self force.....	23
5.6	Raw output of Diener, Warburton, and Wardell code for DG order 44. Time component of the self force. ....	23
5.7	Raw output of Diener, Warburton, and Wardell code for DG order 44. Phi component of the self force.....	24
6.1	$g(\alpha)$ .....	26
6.2	DG convergence with order, extrapolated from highlighted points to infinite order along exponential form, which appears as a straight line in the semilog plot. ....	27
6.3	Starting order was chosen by iterating from the lowest order to the first order for which the “mode failed”, and choosing the maximum starting order that succeeded. When $F_{\text{inf}}$ is evolved over one full orbital cycle, some l-modes shows discontinuities at some times. $l=3$ .....	28
6.4	Fluctuation in one of the points chosen in the extrapolation, due to roundoff or truncation error, causes the extrapolation to predict a value of $F_{\text{inf}}$ that is subtly wrong, leading to curvature in the semilog plot after $F_{\text{inf}}$ subtraction. $t=632$ , $l=2$ , $i=1$ .....	29
6.5	Roundoff error is visible at high DG orders. $t=632$ , $l=2$ , $i=2$ .....	30

6.6	The incorrect value of $F_{\text{inf}}$ has been chosen due to roundoff error, perhaps due to finite precision in the root finding algorithm, leading to a negative values, that show as a “V” in the semilog plot. $t=632$ , $l=3$ , $i=3$ .....	31
6.7	Manual correction for the discontinuities in the $l=2$ mode, using the manually determined $F_{\text{inf}}$ data from Table 6.1. ....	32
6.8	An example of no discontinuities in $F_{\text{inf}}$ for any of the $l$ -modes. Mode $l = 0$ . ....	33
6.9	$l=0$ mode with line-segment fit-chosen starting order produces convergence plot with long exponentially converging region .....	34
7.1	Three term fit of $l$ -mode vs $F_{\text{inf}}$ . Note how the fit is bad at high $l$ . There are an infinite number of additional terms that can be added to the fit to account for this deviation. However, it is also fundamentally difficult to fit an exponentially converging function. See Chapter 8.1. ....	36
7.2	This is the actual summed, doubly extrapolated, radial self force, measured in three different ways as described in the three figures above. ....	37
7.3	$t=635$ , 2, 3, and 4 term fits over a broad range of $l_{\text{min}}$ and $l_{\text{max}}$ values. Note the roundoff noise at high $l_{\text{max}}$ . Aphelion, where this effect is worst. ....	38
7.4	$t=635$ , 2, 3, and 4 term fits over a small range of $l_{\text{min}}$ and $l_{\text{max}}$ . This is the actual range used to estimate the total self force. Aphelion, where the roundoff noise is worst. Note that there is not a large difference between two and three terms, and that four terms is less smooth a surface, suggesting that it is more subject to round off noise. Three terms is preferred. ....	39



7.5	This is the relative difference between the total radial self force measured in two different ways. In both cases, the self force was extrapolated to infinite order at every l-mode at every possible DG starting order. The infinite DG order self forces over the various starting orders were sorted, eliminating NaNs. The median was chosen for each l-mode. Then the self force as a function of l-mode was fit to its three term form, and the sum was summed from zero to lmax, then extrapolated from $l_{max} + 1$ to infinity using an analytic form determined using Mathematica. All possible choices with lmin between 14 and 17 and lmax between 22 and 25 were averaged to obtain the total radial self force as a function of time. Similarly, all possible choices with lmin between 14 and 19 and lmax between 24 and 30 were averaged to obtain the total radial self force as a function of time. This plot shows the relative difference. I believe the smaller range is in the denominator. ....	40
7.6	This figure was produced in the same manner as the previous figure, averaging over the smaller range, only it is a comparison between including either two or three terms in the l-mode fit. I believe the three term fit is in the denominator of the relative difference.....	41
7.7	This figure was produced in a similar manner to the first figure, only instead of using the median, it is a comparison between using the median, the maximum, and the minimum. The purple line is the relative difference between the maximum and the median, which is subject to roundoff error due to the potential for the maximum to contain roundoff error. The green line is the relative difference between the median and the minimum, which is subject to effects due to failure to converge. I suspect the median is the best compromise between these two effects, rejecting outliers in both directions, though it is a simplistic approach to doing so, and does not guarantee success. It is possible to have a starting order that has not converged and is also in the roundoff regime, for example. A better guarantee of success, though not a certain one, would be to do a fit over part of the error convergence plot to determine exponentiality, by fitting a line in semilog scale. However, this seems unnecessarily complex at this time. ....	42
7.8	3 term, median method.....	43
7.9	3 term, fit method.....	43

7.10	The structure of the absolute error in comparison to the evolution in time for the fit method .....	44
8.1	t=570, l=1, three term fit with two different power law scales for weights in comparison to unscaled weights ( $\sigma = 1$ ). .....	46
8.2	The difference between the triangles and the circles shows that the difference in the total radial self force between the presence of a $\sigma \sim l^{-2}$ weight and no weight is unimportant compared to the difference in the total radial self force between various start and end points of the l-mode fit. ....	47
8.3	Absolute error between fit and median techniques increases with l-mode, explaining why the difference between weight and no weight fit techniques is unimportant. ....	48

# Abstract

Insert the text of your abstract here. Make sure there is one blank line between the end of the Abstract text and the “end” command below to maintain double-spaced lines.

# Chapter 1

## Introduction

### 1.1 Gravitational Waves

On February 11, 2016, the LIGO Scientific Collaboration announced the first detection of gravitational waves from a black hole binary inspirals, occurring on September 14, 2015, with pre-merger masses of  $36 M_{\odot}$  and  $29 M_{\odot}$  and a post merger mass of  $62 M_{\odot}$  at a redshift of  $z = 0.09$  [33]. Two subsequent detections followed, on December 26, 2015 [34] and on January 4, 2017 [35], with masses that are about the same to within an order of magnitude.

There is a question of what is meant, observationally, by a black hole. Does it need to have a horizon? Does it need to have a Kerr metric (the simplest possible space-time for a spinning black hole in general relativity)? Does it simply need to be a sufficiently compact object that it can't be ordinary nuclear matter? Historically, black holes have been defined by their compactness [47]; however, some studies are beginning to consider tests of horizons [] or of the Kerr metric itself [47]. X-ray binaries, gravitational wave constraints from binary-pulsar systems, active galactic nuclei models containing super-massive black holes on the order of  $10^6 M_{\odot}$ , and the three LIGO detections, as well as black hole formation models, suggest that black holes of all scales should be spinning [47]. However, for the purposes of this manuscript, I will consider non-spinning, spherically symmetric black holes in general relativity, described by the Schwarzschild metric.

Currently, there are four distinct windows on the gravitational wave universe planned or in progress. The Laser Interferometer Gravitational Wave Observatory, LIGO, probably deserves first listing, due to their recent success. LIGO observes gravitational waves using a ground based Michelson-Morley interferometer with two 4 kilometer long Fabry-Perot cavity arms. It detects strains as small as  $10^{-23} Hz^{-1/2}$  [48].

- 1.2 Extreme Mass Ratio Inspirals
- 1.3 EMRIs
- 1.4 The discontinuous galerkin method
- 1.5 LISA

# Chapter 2

## A simple numerical solution for a PDE using the Discontinuous Galerkin method

### 2.1 Reduction to coupled first order differential equations

The fundamental problem we wish to solve is to evolve the wave equation on Schwarzschild spacetime with a source. However, to begin to address this problem, I implemented a one dimensional wave equation solver in C++ using the Discontinuous Galerkin method in flat spacetime. The wave equation in flat spacetime is given, in several different forms, by

$$\square\psi = 0 \tag{2.1}$$

$$\frac{\partial^2\psi}{\partial t^2} = \nabla\psi \tag{2.2}$$

$$\frac{\partial^2\psi}{\partial t^2} = \frac{\partial^2\psi}{\partial r^2} \tag{2.3}$$

where the final form is specialized to one dimension. To numerically integrate this, it is necessary to reduce this second order differential equation to three coupled differential first order differential equations. There is a classical solution to this problem, which we follow. We introduce variables  $\rho = \frac{\partial\psi}{\partial t}$  and  $\phi = \frac{\partial\psi}{\partial r}$ . With these definitions, and remembering that we want time evolution equations rather than spatial evolution equations, the three coupled equations become

$$\frac{\partial\psi}{\partial t} = \rho \tag{2.4}$$

$$\frac{\partial\rho}{\partial t} = \frac{\partial\phi}{\partial r} \tag{2.5}$$

$$\frac{\partial\phi}{\partial t} = \frac{\partial\rho}{\partial r} \tag{2.6}$$

This system of equations can be rewritten

$$\frac{\partial u}{\partial t} = A \frac{\partial u}{\partial r} + B \frac{\partial u}{\partial t} = RHS(u, t)$$

where  $u$  is the state vector consisting of  $u = (\psi, \rho, \phi)$ , and  $A$  and  $B$  are matrices. RHS stands for Right Hand Side. The C++ code has been implemented for wave equations of this generalized form, which encompasses wave equations on a Schwarzschild spacetime.

## 2.2 Spatial grids

Our code solves a wave equation, which must first calculate a spatial derivative then integrate in time to solve a differential equation. For the spatial derivative part of the scheme, we make use of the Discontinuous Galerkin method to compute spatial derivatives, as a replacement for a finite difference scheme. It has three primary benefits. One is that it naturally handles discontinuities in the evolved field, which is important to the effective source approach that we use when calculating orbits with a source in curved spacetime. The second is that its accuracy scales exponentially with increasing polynomial order. The third is that its accuracy scales as a power law with decreasing element size, giving a second strong way to reduce the truncation error.

### 2.2.1 Finite difference schemes

The classic solution to the spatial derivative problem is the finite difference scheme. In a one dimensional finite difference scheme, space is discretized into points on a line. The spatial derivative is calculated using a stencil of points that is symmetric about the point where one wants to know the spatial derivative, and extends  $n - 1$  points beyond to either side, where  $n$  is the order of the expansion. The spatial derivative is calculated from a weighted sum of the points included in the stencil, where some of the weights are negative. A stencil with  $2n - 1$  points in it, in one dimension, corresponds to an  $n$ th order expansion. It is possible to expand any order of derivative to any order of expansion. A first derivative,

to second order accuracy, given by:

$$D_r^{(2)} = \frac{1}{h} \left( -\frac{1}{2}f_{-1} + \frac{1}{2}f_1 \right) \quad (2.7)$$

Here the  $f_{-1}$  and  $f_1$  indicate the function evaluated at the grid point to either side of the 0th grid point, where the derivative is evaluated. Here  $h$  is the spacing between grid points.

A first derivative, to third order accuracy, is given by:

$$D_r^{(3)} = \frac{1}{h} \left( \frac{1}{12}f_{-2} - \frac{2}{3}f_{-1} + \frac{2}{3}f_1 - \frac{1}{12}f_2 \right) \quad (2.8)$$

Notice how no first order derivative includes the central point in its stencil. In contrast, a second derivative to second order accuracy is given by:

$$D_r^{(2)} = \frac{1}{h^2} (f_{-1} - 2f_0 + f_1) \quad (2.9)$$

This derivative is symmetric, while the first derivative is antisymmetric.

It is possible to extend these stencils to two and three dimensions. When considering parallelization using OpenMP, issues of synchronization must be considered. When parallelizing over many nodes, the spatial grid gets divided into blocks. At the ends of each block, the boundary cells need information from the neighboring cells to calculate the spatial derivative. For an order  $n$  derivative,  $n - 1$  boundary cells are synchronized into buffer zones both to the left and to the right at each time step. In our code, this is not necessary, since we have parallelized with OpenMP, which uses shared memory within one node, across several (16) cores.

### 2.2.2 The Discontinuous Galerkin method

The Discontinuous Galerkin method breaks space into segments called elements. Within each element, the value of the field is represented by the sum of  $n$  interpolating polynomials of order  $n$ , where  $n$  is the order of the element. There are  $n + 1$  unevenly spaced nodes



in the element, clustered toward the edges. At each node, exactly one of the interpolating polynomials takes on a value of one while the others are zero. An interpolating Lagrange polynomial has a functional form:

$$\ell_i(r) = \prod_{j=1, j \neq i}^n \frac{r - \xi_j}{\xi_i - \xi_j} \quad (2.10)$$

where  $\xi_i$  is a location of a node and where  $r$  is an arbitrary position [50].

Omitting the details of the derivation of this method, which can be found in Reference [50], the procedure for calculating the spatial derivative in one dimension is to first calculate the Legendre polynomials, rescaled by a factor depending upon their order.  $\tilde{P}_n(r) = \frac{P_n(r)}{\sqrt{\gamma_n}}$  where  $\gamma_n = \frac{2}{2n+1}$ . The following procedure of differentiation and matrix inversion can be used to calculate the derivative matrix for each element,  $D_r$  [50].

$$V_{ij} = \tilde{P}_j(r_i) \quad (2.11)$$

$$V_{r,(i,j)} = \left. \frac{d\tilde{P}_j}{dr} \right|_{r_j} \quad (2.12)$$

$$V^T D_r^T = (V_r)^T \quad (2.13)$$

In practice, we use a custom package, the Template Numerical Toolkit (TNT) library and JAMA, to invert the equation using LU decomposition. Beware! TNT and JAMA are not thread safe, and cannot be used with shared memory parallelization. They result in race conditions, and it was ultimately necessary to rewrite the parallelized portion of the code to avoid the TNT classes.

The Discontinuous Galerkin method helps damp error introduced by discontinuities in the field, provided they remain at element boundaries. We make use of this in our self-force calculations in the neighborhood of the particle, to be described in Chapter 5.0.2. The numerical flux is a way of accounting for the discontinuity in the flow between neighboring elements. There are multiple ways of calculating this flux, but in our code, we use a version

relevant to linear hyperbolic problems, such as Equation 2.7, which, recall, is specialized to a one-dimensional problem. In this case,  $A = S\Lambda S^{-1}$ , for some transformation matrix  $S$ , where  $\Lambda$  is a diagonal matrix. Let  $\Lambda^+$  and  $\Lambda^-$  be the positive and negative eigenvalues of  $\Lambda$ , respectively, corresponding to the outgoing and ingoing waves. Then the numerical upwind flux is given by

$$(\hat{n}\dot{F}) = S(\Lambda^+ S^{-1} u^- + \Lambda^- S^{-1} u^+) \quad (2.14)$$

This flux, based upon the state vector interior to  $(u^-)$  and exterior to  $(u^+)$  the element, at each end of the element, is distributed across the whole element from end to end via the lift matrix [50].

## 2.3 Time evolution

Time evolution in our code is handled by a fourth order low storage Runge Kutta method. Instead of the standard fourth order Runge Kutta method, this method takes five sub-timesteps, but only the most recent sub-timestep needs to be stored.

$$p^{(0)} = u^n k^{(i)} = a_i k^{(i-1)} + \delta t RHS(p^{(i-1)}, t^n + c_i \delta t) p^{(i)} = p^{(i-1)} + b_i K^{(i)} u_h^{n+1} = p^{(5)} \quad (2.15)$$

Here steps two and three are repeated for  $i = 1 - 5$ , first  $k$ , then  $p$ , then increase  $i$  and repeat. The coefficients  $a_i$ ,  $b_i$ , and  $c_i$  are given in Reference [50].

## 2.4 Wave equation on flat spacetime

Using gaussian initial conditions in  $\psi$  and setting the  $\rho$  initial conditions to the derivative of that gaussian, I have produced the evolution shown in Figure 2.1. The gaussian marches to the right over a number of time steps, hits the periodic boundary conditions, and re-enters the one-dimensional space on the left, eventually returning to its original position. A similar progression can be seen in Figure 2.2 for sinusoidal initial conditions.

The Discontinuous Galerkin method has truncation error that scales as  $h^{n+1}$ , where  $h$  is the element size and  $n$  is the polynomial order of the elements. The  $L_2$  error is defined

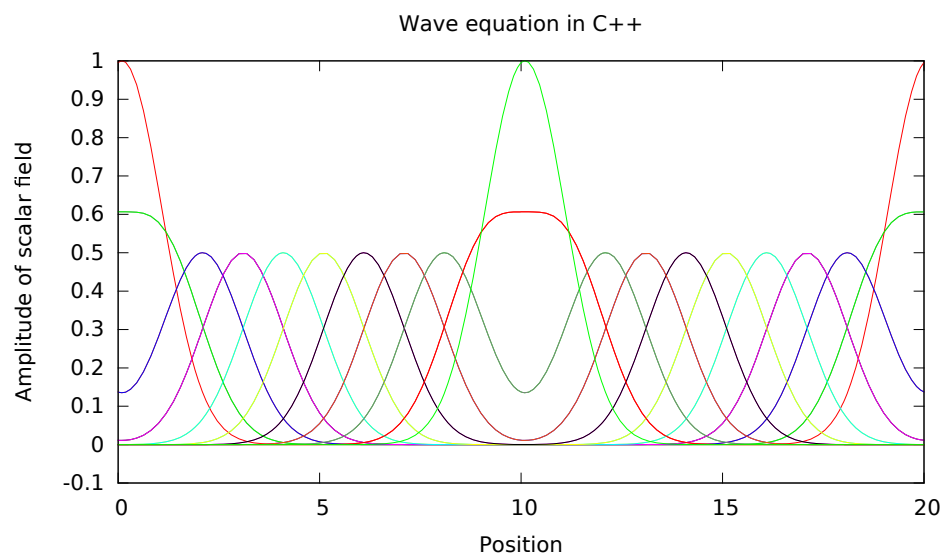


Figure 2.1: Waves evolving over time for gaussian initial conditions

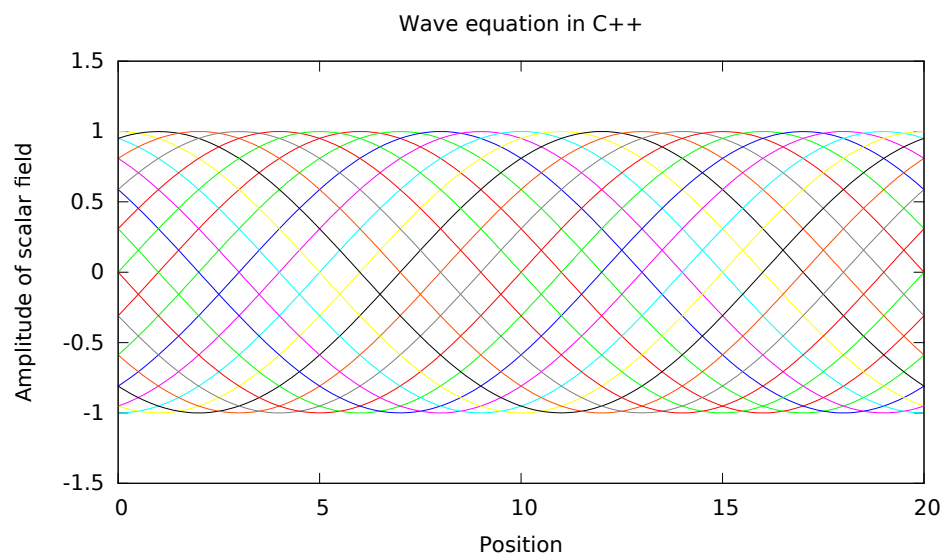


Figure 2.2: Waves evolving over time for sinusoidal initial conditions

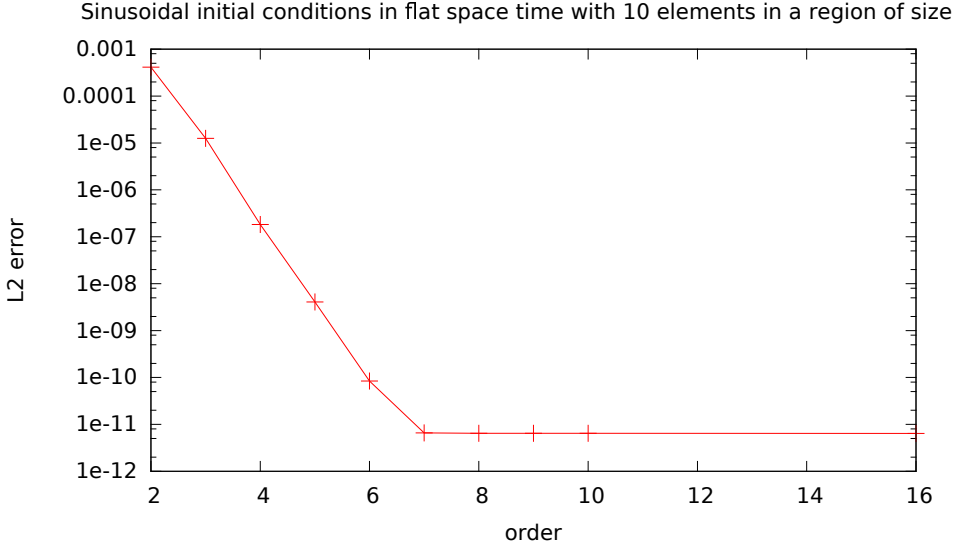


Figure 2.3:  $L_2$  error scaling with DG order for sinusoidal initial conditions

as the square root of the sum of the squared differences across all space, after one complete cycle of the system. The scaling of the  $L_2$  error with DG order and with element size is shown in Figures 2.3 and 2.4. The scaling matches expectations until roundoff error is hit, where the error stops improving with order or smaller element size. Not shown, this same pattern was seen for the  $L_0$  error, which is the maximum error over all space.

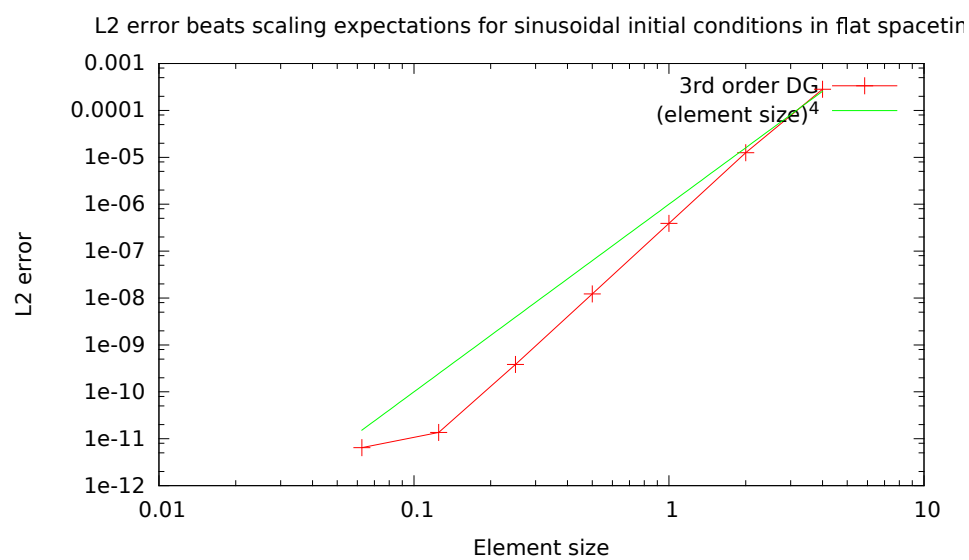


Figure 2.4:  $L_2$  error scaling with element size for sinusoidal initial conditions

# Chapter 3

## A scalar field on a Schwarzschild background without a source

### 3.1 Scalar field on Schwarzschild spacetime

#### 3.1.1 Multipole moment decomposition

#### 3.1.2 Hyperboloidal compactification

Tortoise coordinates and wave equation Wave equation in this form Boundary conditions

#### 3.1.3 Initial conditions

#### 3.1.4 final results

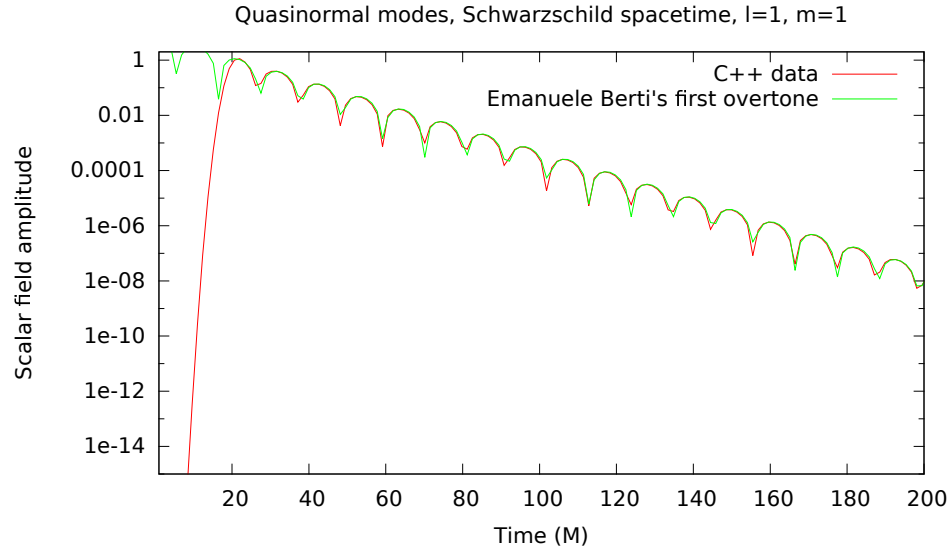


Figure 3.1: Quasinormal mode for  $l=1, m=1$

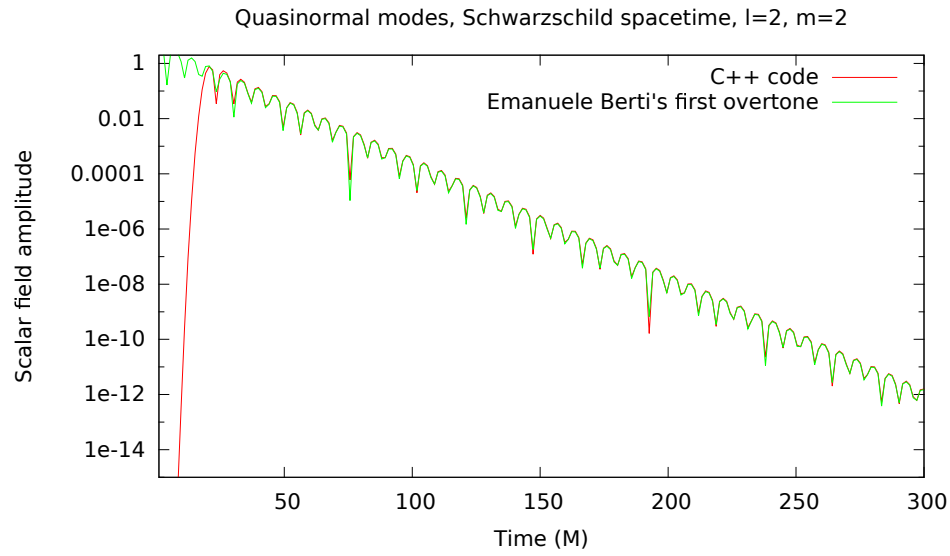


Figure 3.2: Quasinormal mode for  $l=2, m=2$

The C++ code, and Richard Price's theoretical expectation for the power law tails,  $l=1$

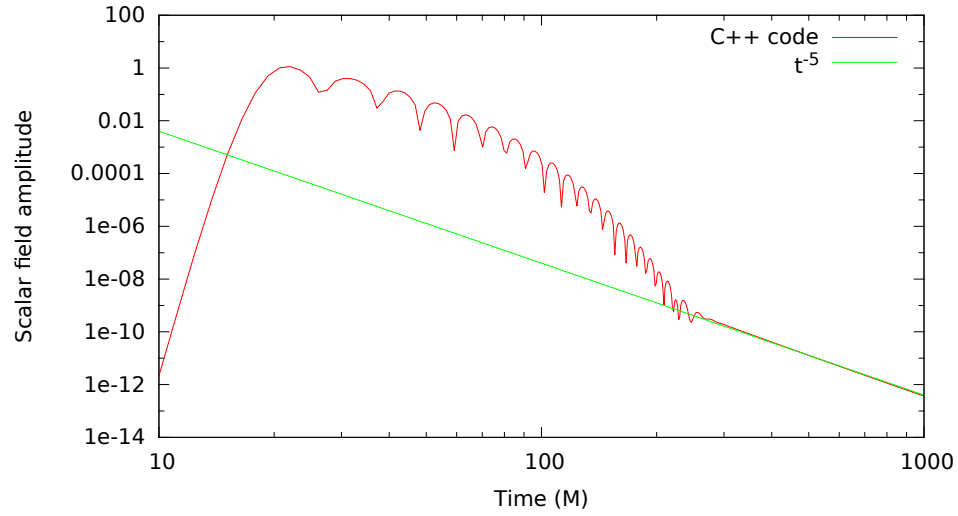


Figure 3.3: Power law tail,  $l=1$ ,  $m=1$

The C++ code, and Richard Price's theoretical expectation for the power law tails,  $l=2$

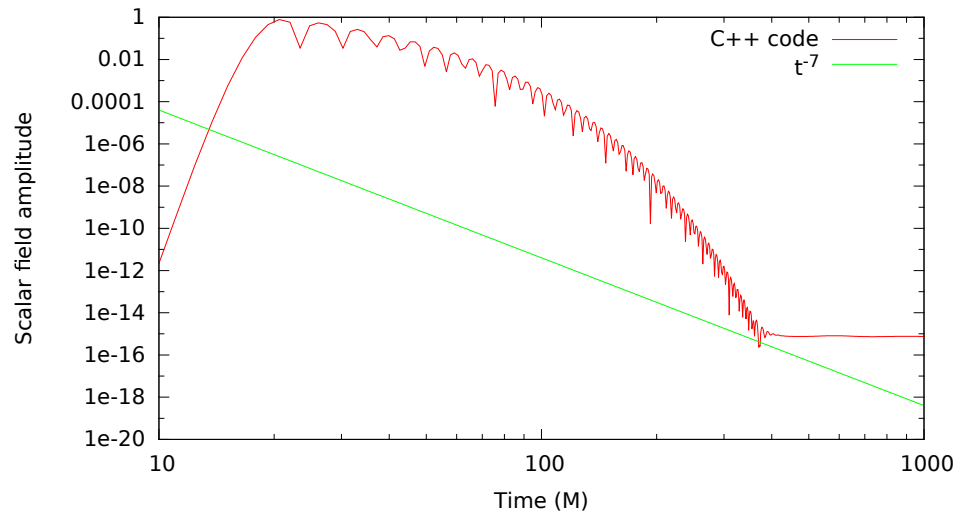


Figure 3.4: Power law tail does not match expectations due to truncation error in DG method,  $l=2$ ,  $m=2$



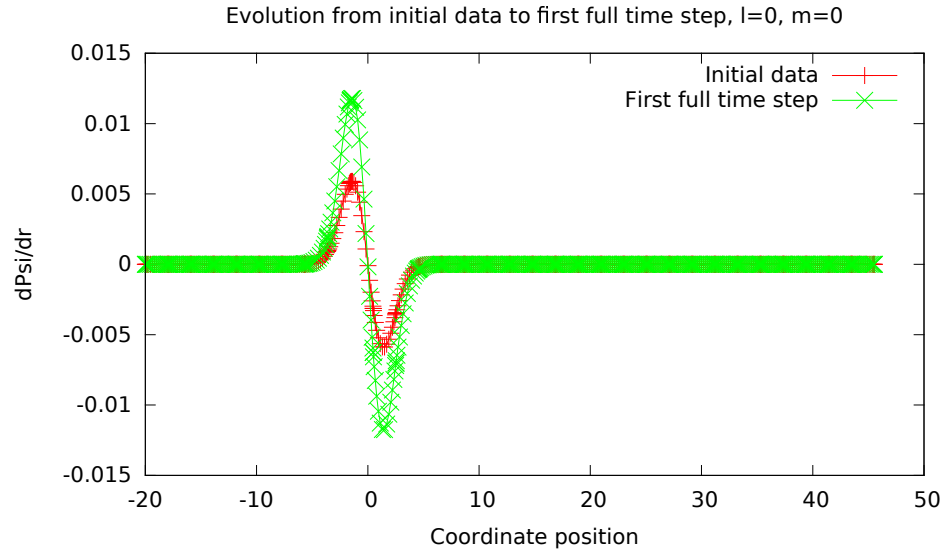


Figure 3.5: Scalar field spatial slice initial condition and first full timestep for  $l=0$ .

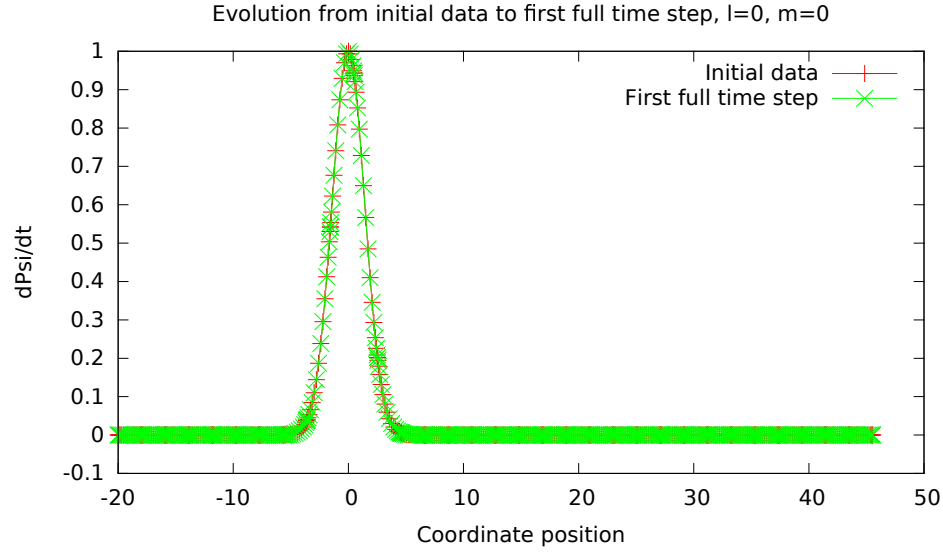


Figure 3.6: Time derivative of the scalar field spatial slice initial condition and first full timestep for  $l=0$ .

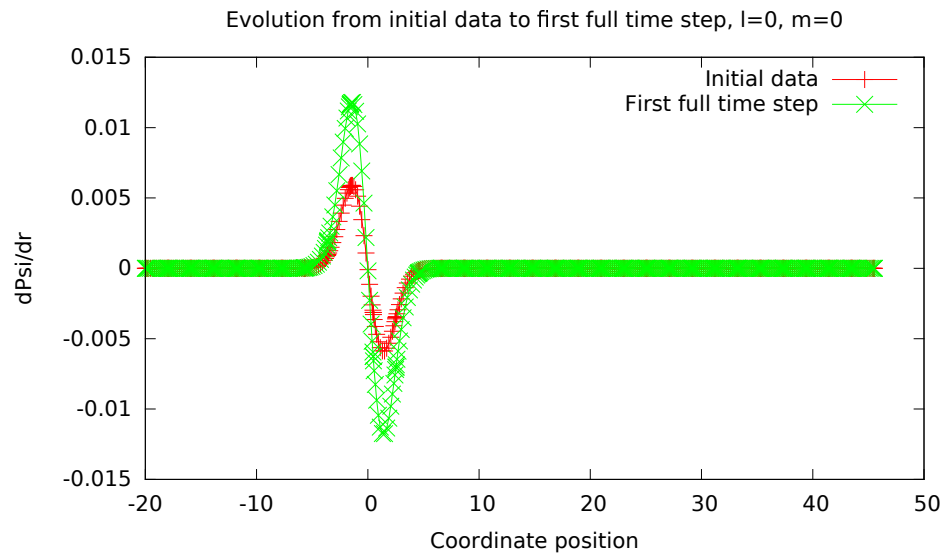


Figure 3.7: Radial derivative of the scalar field spatial slice initial condition and first full timestep for  $l=0$ .

# Chapter 4

## Circular orbits on a Schwarzschild spacetime

### 4.1 $\phi$ of $t$

#### 4.1.1 Effective source

#### 4.1.2 World tube

#### 4.1.3 Comparison between C++ and Fortran codes

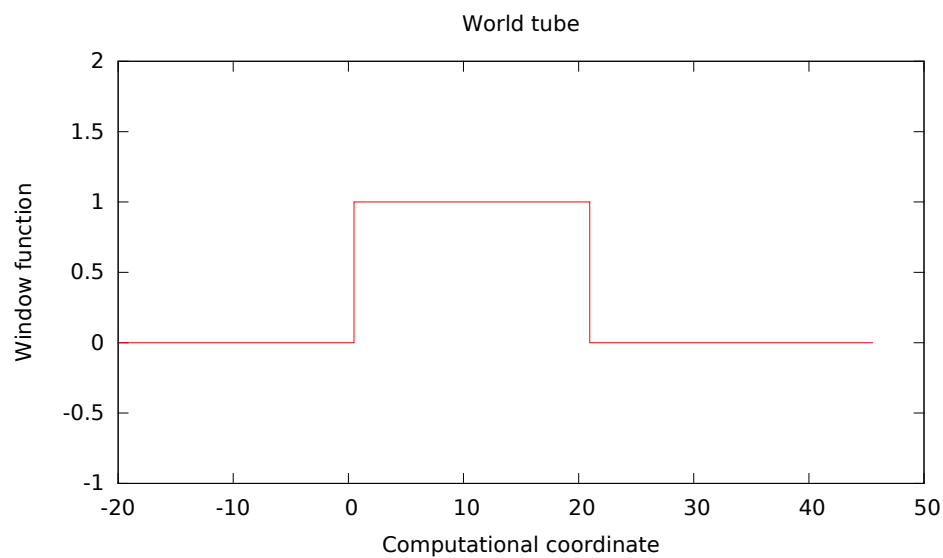


Figure 4.1: Spatial slice of the world tube window function.

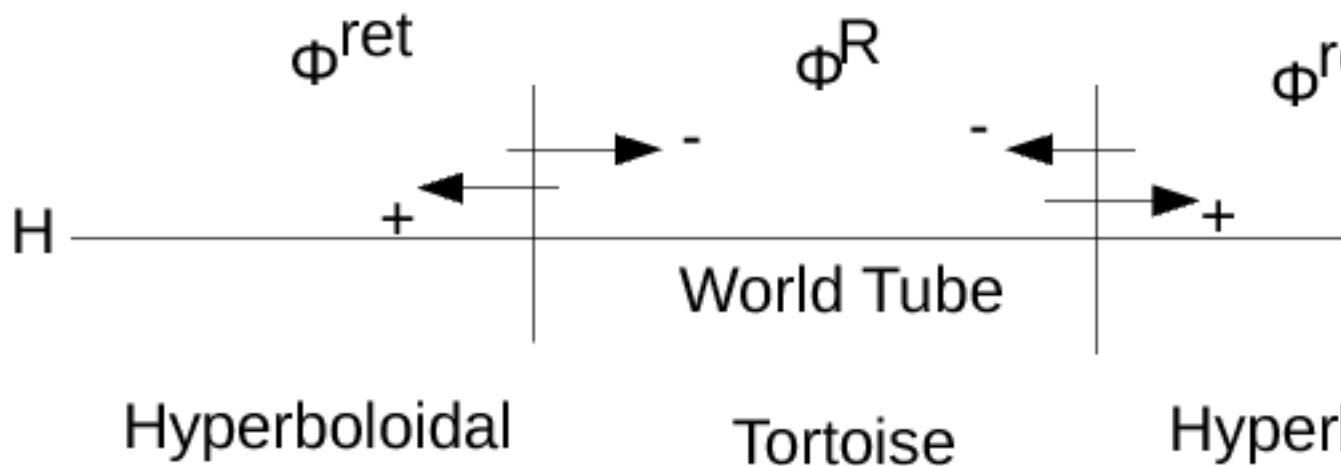


Figure 4.2: Add or subtract the singular field to either side of the world tube boundary before performing the time dependent coordinate transform (or inverting it) to obtain the retarded field in the exterior region and the regularized field in the interior region.

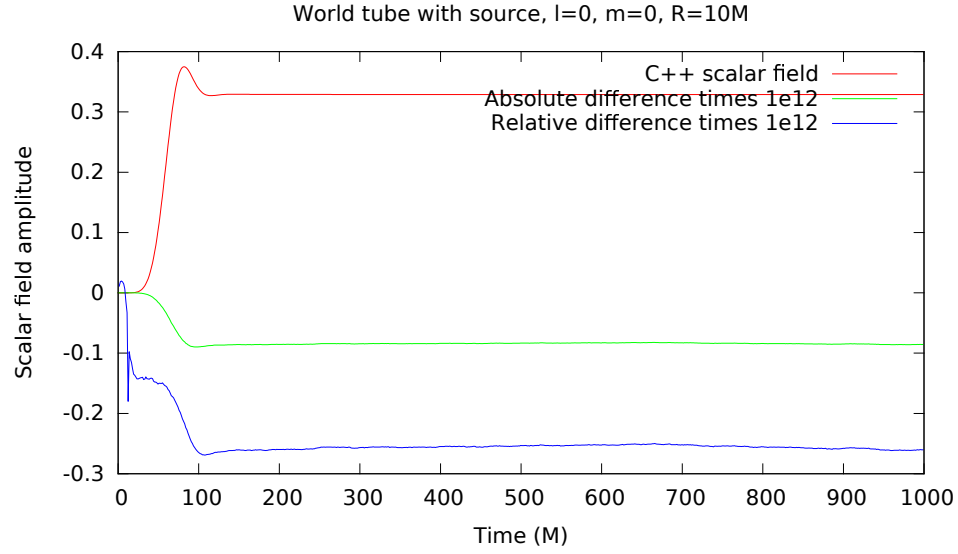


Figure 4.3: Comparison between Fortran and C++ codes for a particle on a circular orbit,  $l=0$ ,  $m=0$ .

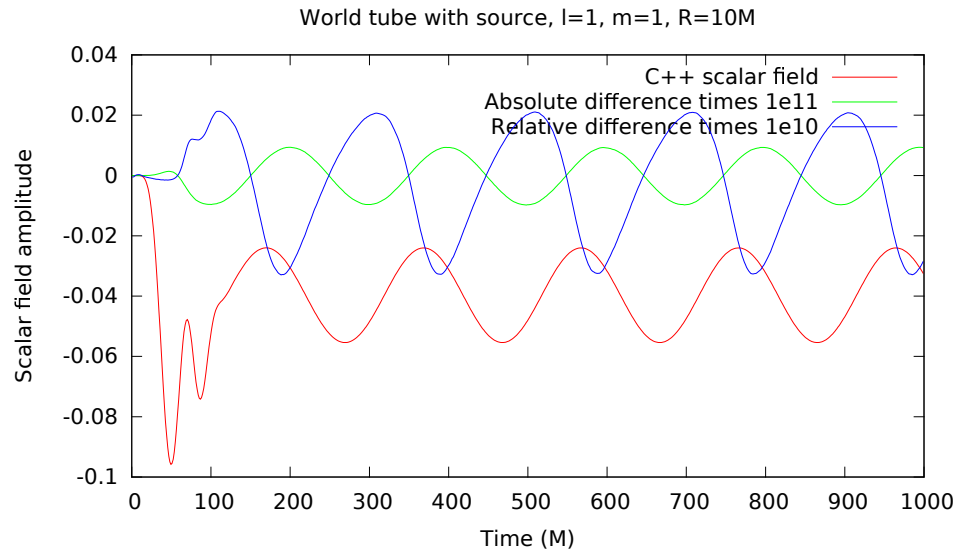


Figure 4.4: Comparison between Fortran and C++ codes for a particle on a circular orbit,  $l=1$ ,  $m=1$ .

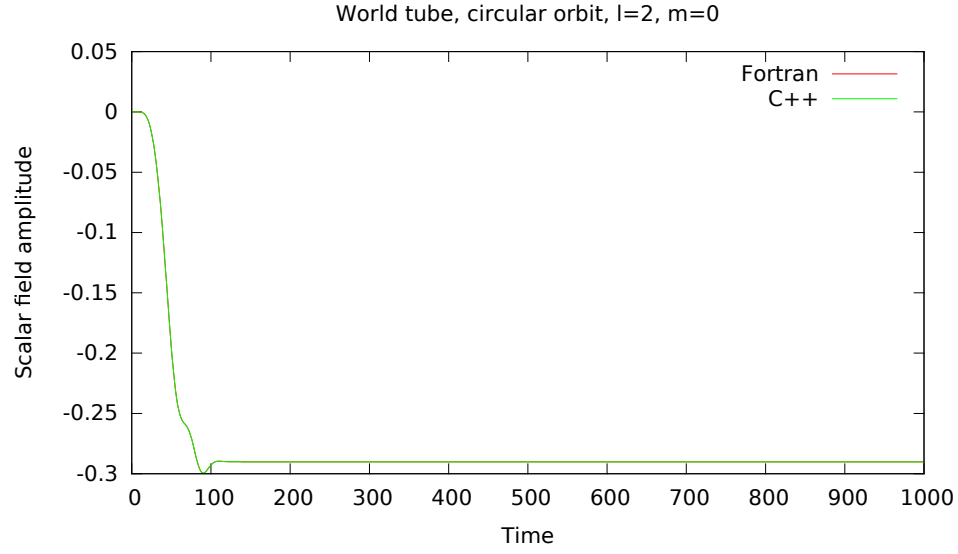


Figure 4.5: Comparison between Fortran and C++ codes for a particle on a circular orbit,  $l=2$ ,  $m=0$ .

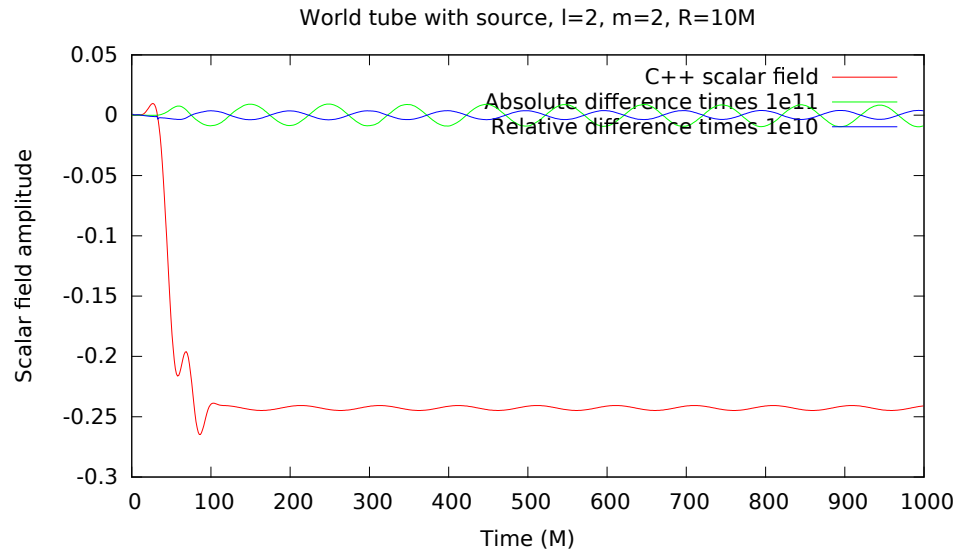


Figure 4.6: Comparison between Fortran and C++ codes for a particle on a circular orbit,  $l=2$ ,  $m=2$ .

# Chapter 5

## Elliptical orbits on a Schwarzschild spacetime

### 5.0.1 Time dependent coordinate transformation

wave equation

### 5.0.2 orbital parameters (osculating orbits paper)

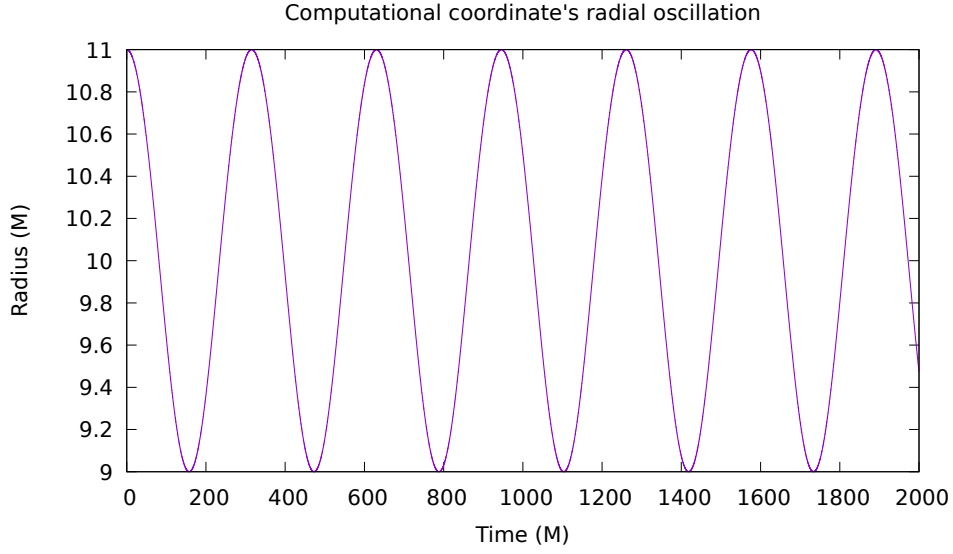


Figure 5.1: Schwarzschild  $r$  as a function of time over several orbits.

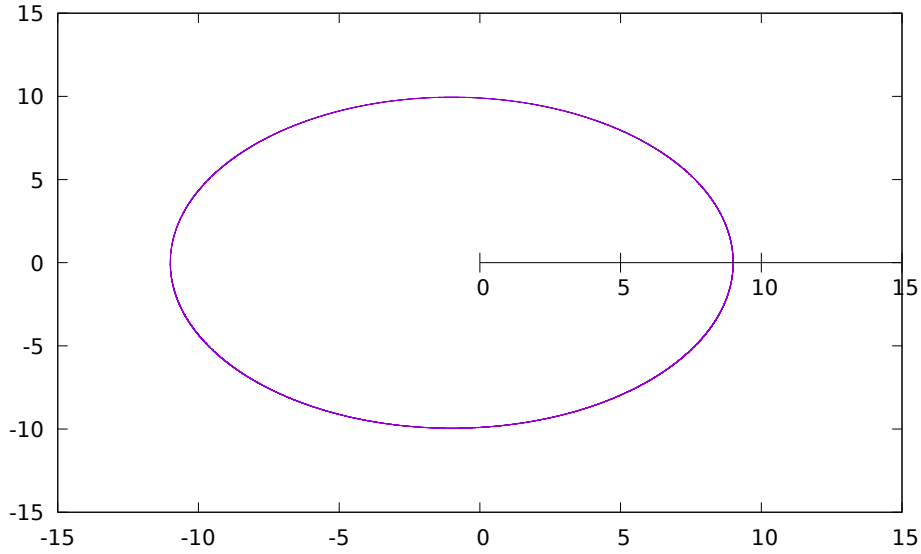


Figure 5.2: Plotting  $\chi$  as the angle in polar coordinates, the orbit forms an exact ellipse. This is the definition of  $\chi$ , provided  $r$  is in Schwarzschild coordinates. Shown for  $p = 9.9$  and  $e = 0.1$ , DG order 44



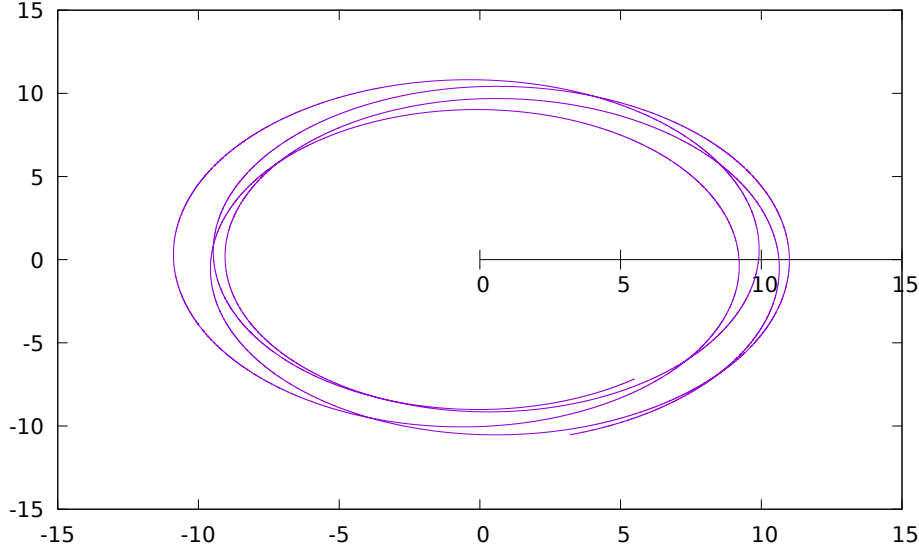


Figure 5.3: Plotting the orbit as it physically would exist, using Schwarzschild  $\phi$  as the polar coordinate angle, the orbit precesses but does not inspiral since there is no generic evolution yet. Shown for  $p = 9.9$  and  $e = 0.1$ , DG order 44

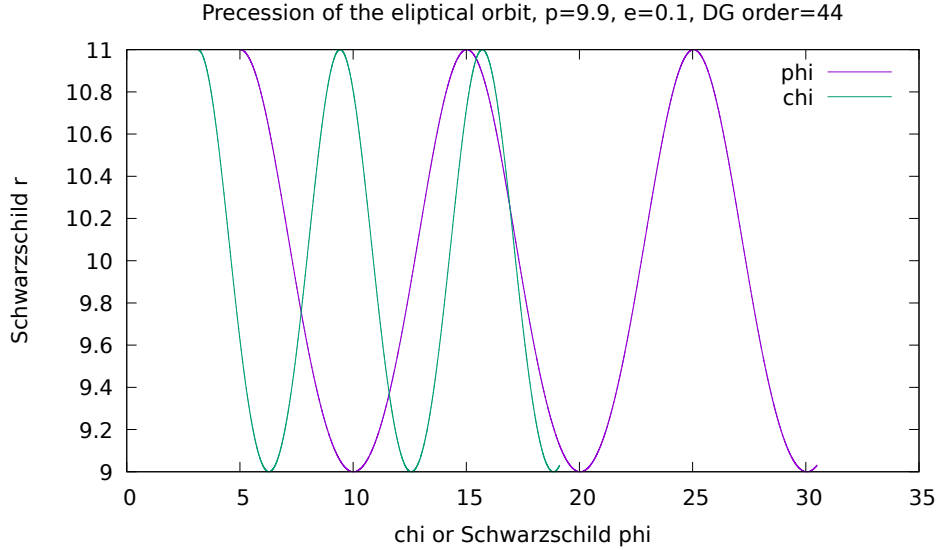


Figure 5.4: Precession of the elliptical orbit is demonstrated due to the inequality in the period of the angular variables  $\chi$ , which represents the period of the radial oscillations, and  $\phi$ , which represents the period of the angular oscillations.  $p = 9.9$ ,  $e = 0.1$ , DG order 44.

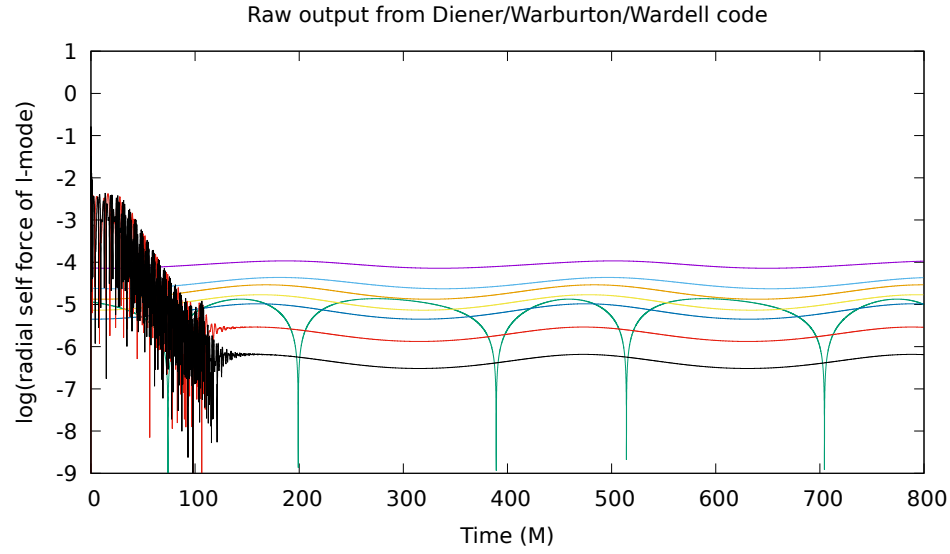


Figure 5.5: Raw output of Diener, Warburton, and Wardell code for DG order 44. Radial self force.

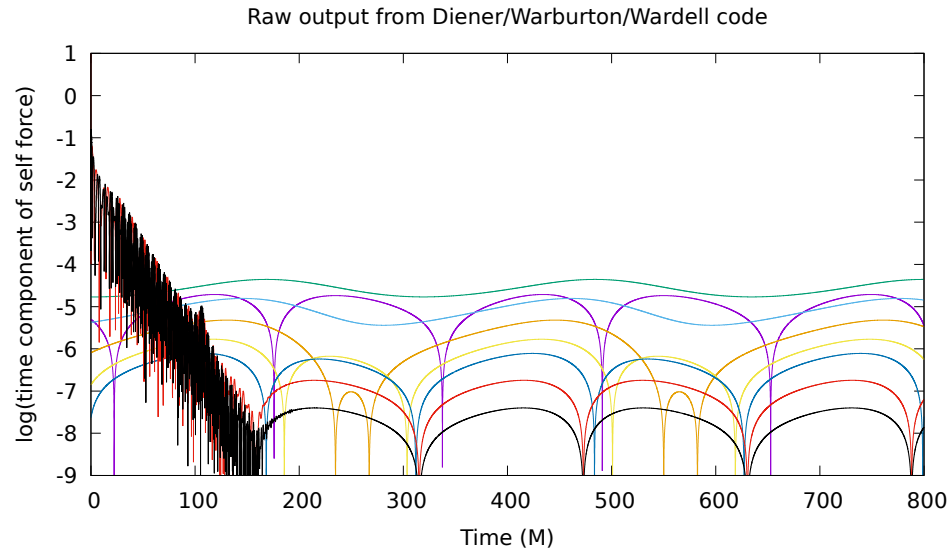


Figure 5.6: Raw output of Diener, Warburton, and Wardell code for DG order 44. Time component of the self force.

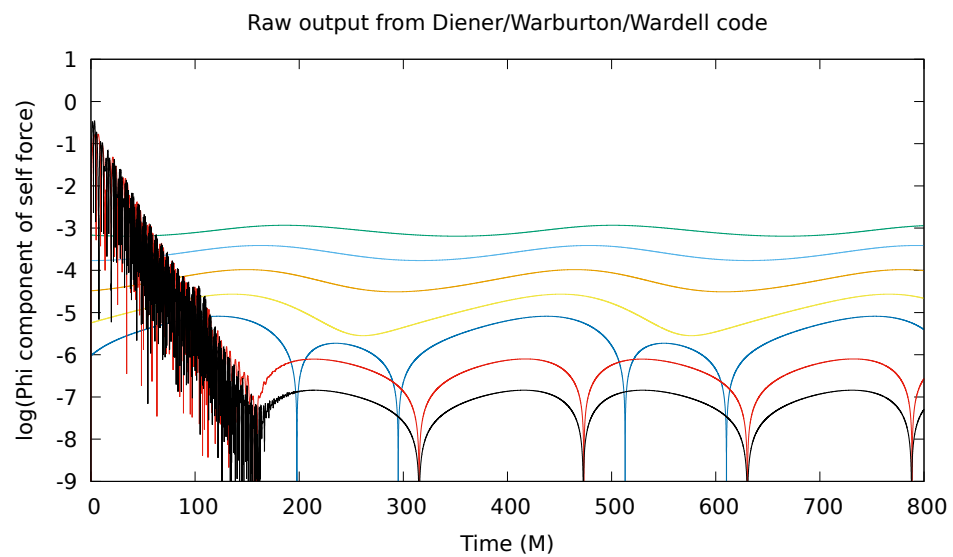


Figure 5.7: Raw output of Diener, Warburton, and Wardell code for DG order 44. Phi component of the self force.

# Chapter 6

## Extrapolating the self force to infinite Discontinuous Galerkin order

The Discontinuous Galerkin method results in truncation error that scales as  $h^{N+1}$ , where  $h$  is the element size and  $N$  is the order of the interpolating polynomials within the element. [50] The self force is given by the radial derivative of the

Note that it is not always possible to choose three points such that they lie on a converging exponential form, for instance, if they are not monotonic, or if they curve in the wrong direction. In these cases, I say that the “mode failed”, and discard the result for that mode with that starting order for the extrapolation. I use extrapolation starting orders from the set 12, 16, 20, 24, 28, 32, and 36, with additional data at orders 40 and 44 that may be used as points two and three in the extrapolation.

### 6.0.1 Checking for discontinuities in $F_{\text{inf}}$ for each each l-mode

In the median approach, the starting orders that did not “fail” at each time and for each mode are ordered by their  $F_{\text{inf}}$  values. The median value of  $F_{\text{inf}}$  is selected, presumably discarding those effected by roundoff and those effected by failure to converge. However, there is no guarantee that it selects those in this regime, since in principle a mode could both be in the roundoff limit and have not converged yet. Yet when this is done, there are no discontinuities in  $F_{\text{inf}}$  for any of the l-modes when the median approach is used. See mode zero for an example.

time	starting order	finf
632	0	mode failed
632	1	2.40975299617e-05
632	2	2.40975300465e-05
632	3	2.40975300114e-05
632	4	mode failed
632	5	2.40975299291e-05
632	6	2.40975299148e-05

Table 6.1: Manual starting indices and  $F_{\text{inf}}$  values for t=632, l=2.

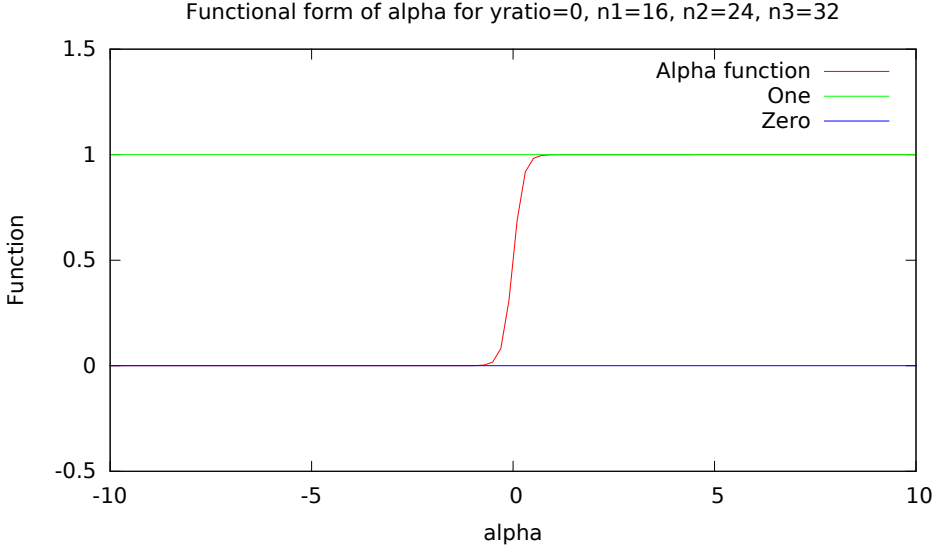


Figure 6.1:  $g(\alpha)$

### 6.0.2 Determining $F_{\text{inf}}$ using maximum likelihood fits to subsegments of lines in semilog space

A better motivated approach, is to fit subsegments of lines in semilog space on the DG order convergence plot, and find the most linear, longest linear, region. A fit with the “best” value of the reduced chi squared should be a good approximation to this. The reduced chi squared is the value of the sum of the residuals of the fit squared divided by the number of degrees of freedom, which in this case is the number of points in the fit minus two, since there are two degrees of freedom in a linear fit. The expectation value of the reduced chi squared, in the limit of a large number of degrees of freedom, is one. I loop over starting and ending points of the fit, and over starting orders, and choose the starting order with the best fit line segment in the sense that that line segment has a reduced chi squared closest to one. An example of such an automatically chosen starting index is given in Figure ??, where there is a long exponentially converging region.

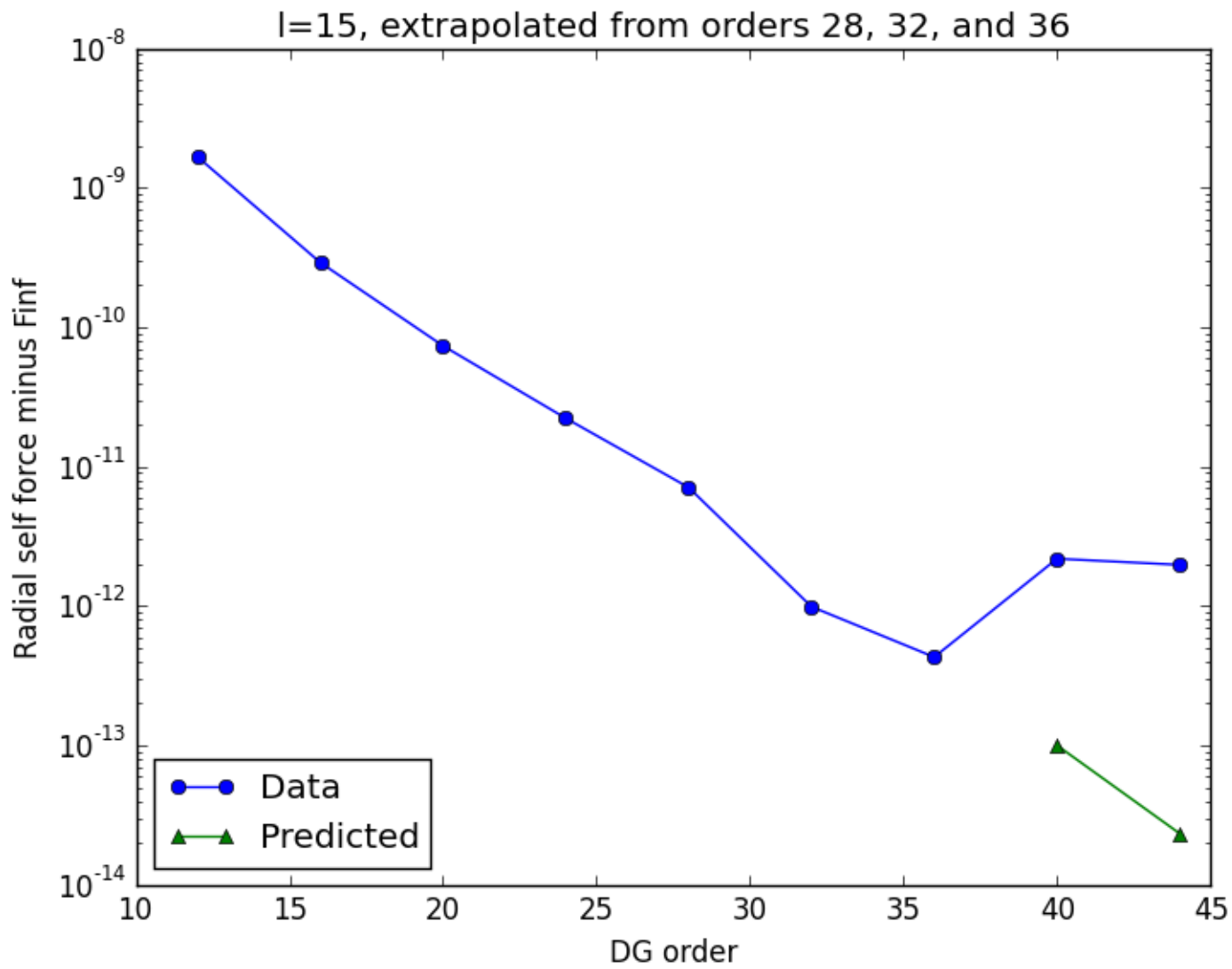


Figure 6.2: DG convergence with order, extrapolated from highlighted points to infinite order along exponential form, which appears as a straight line in the semilog plot.

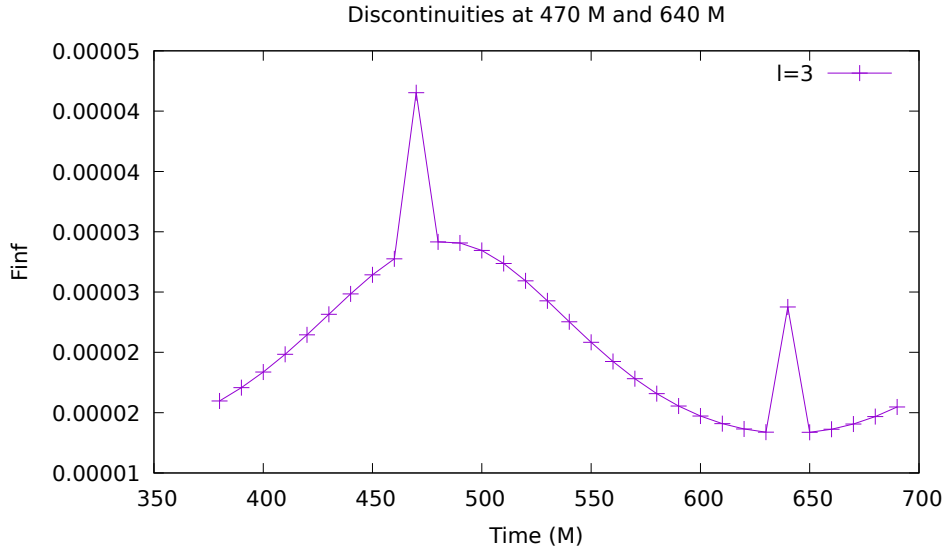


Figure 6.3: Starting order was chosen by iterating from the lowest order to the first order for which the “mode failed”, and choosing the maximum starting order that succeeded. When  $F_{\text{inf}}$  is evolved over one full orbital cycle, some  $l$ -modes show discontinuities at some times.  $l=3$

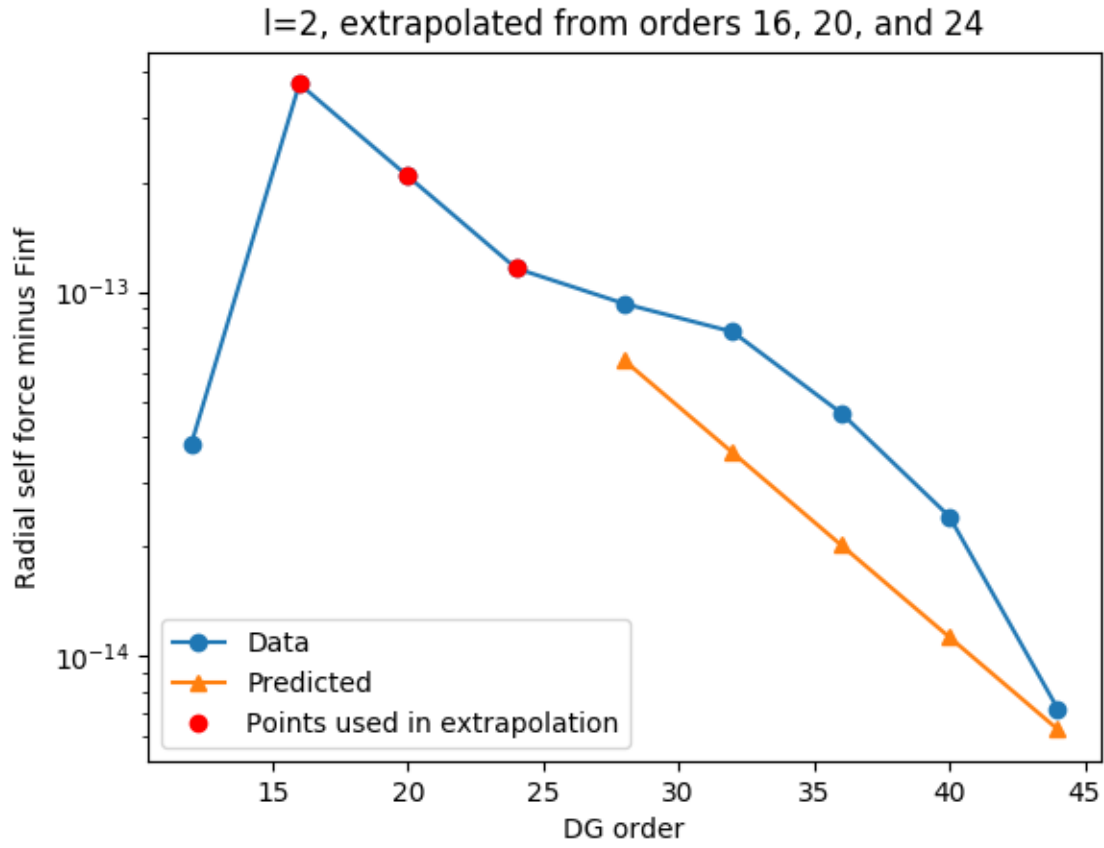


Figure 6.4: Fluctuation in one of the points chosen in the extrapolation, due to roundoff or truncation error, causes the extrapolation to predict a value of  $F_{\text{inf}}$  that is subtly wrong, leading to curvature in the semilog plot after  $F_{\text{inf}}$  subtraction.  $t=632$ ,  $l=2$ ,  $i=1$



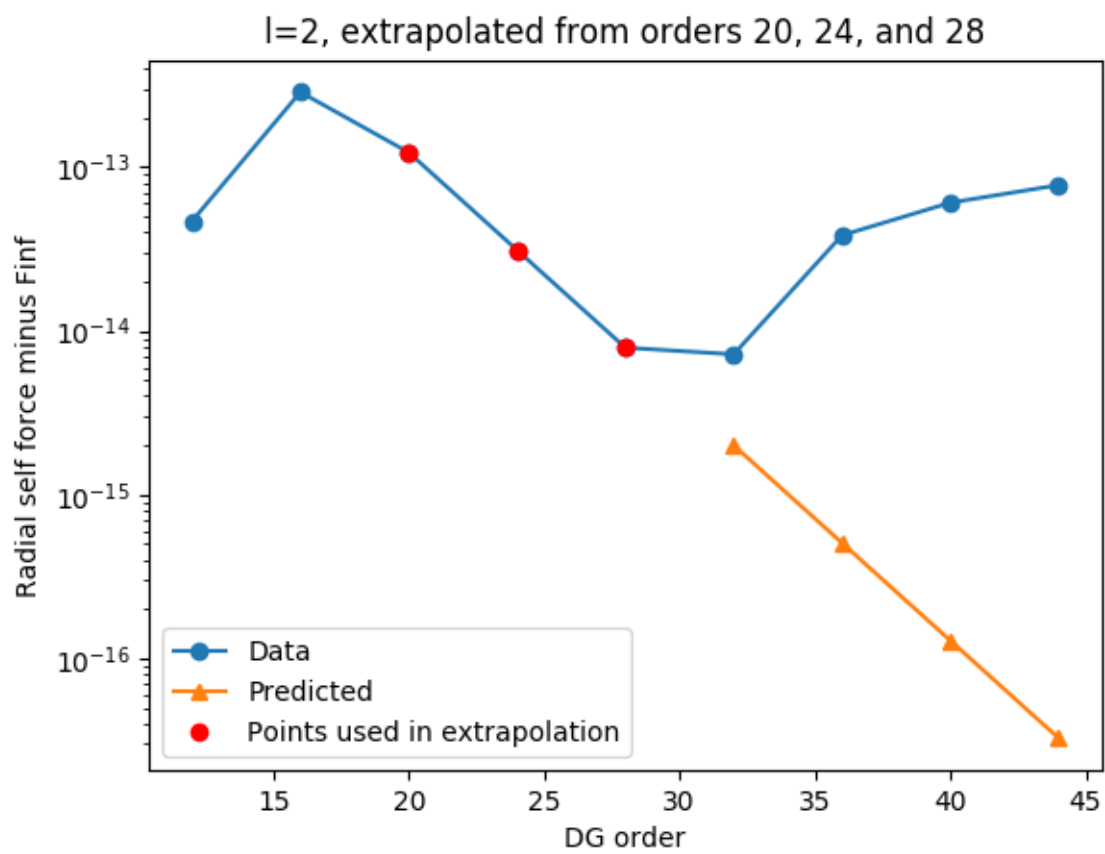


Figure 6.5: Roundoff error is visible at high DG orders.  $t=632$ ,  $l=2$ ,  $i=2$

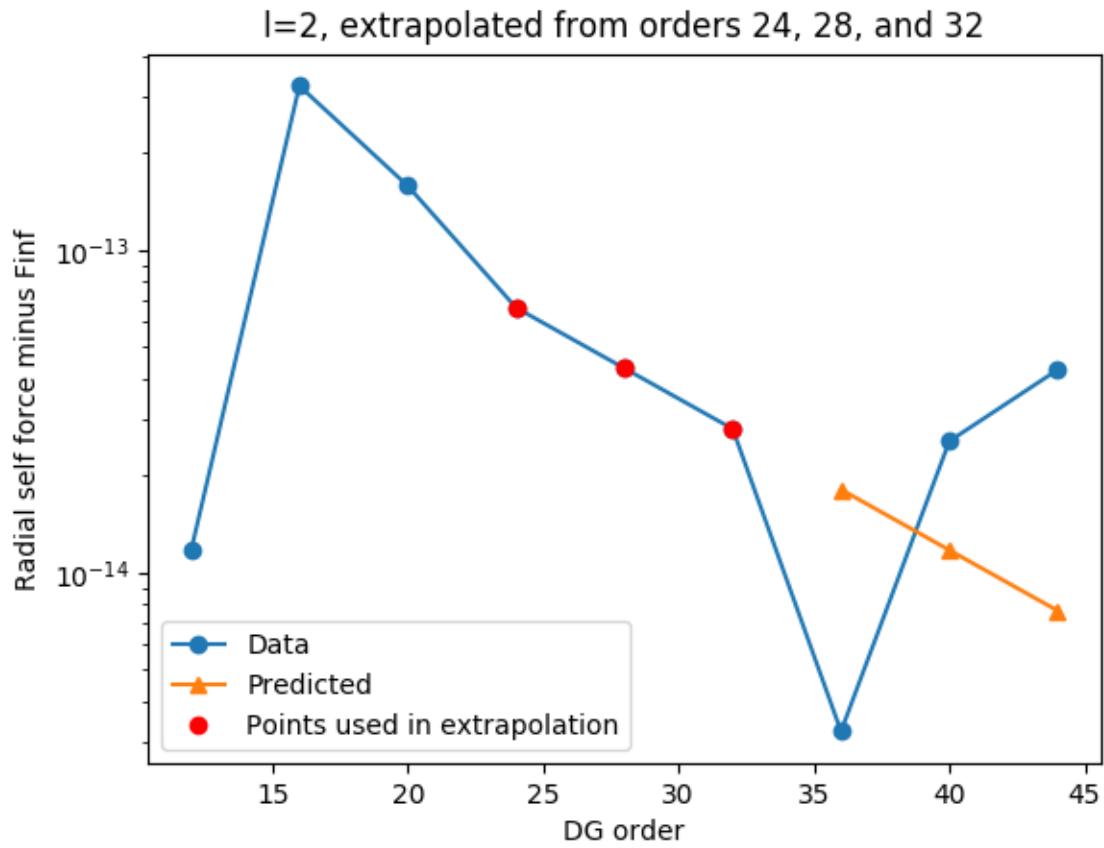


Figure 6.6: The incorrect value of  $F_{\text{inf}}$  has been chosen due to roundoff error, perhaps due to finite precision in the root finding algorithm, leading to a negative values, that show as a “V” in the semilog plot.  $t=632$ ,  $l=3$ ,  $i=3$

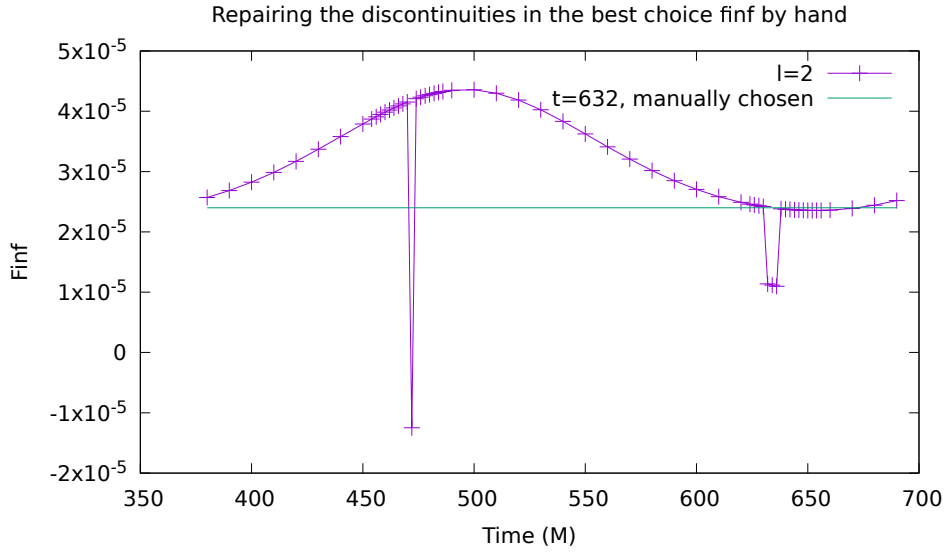


Figure 6.7: Manual correction for the discontinuities in the  $l=2$  mode, using the manually determined  $F_{\text{inf}}$  data from Table 6.1.



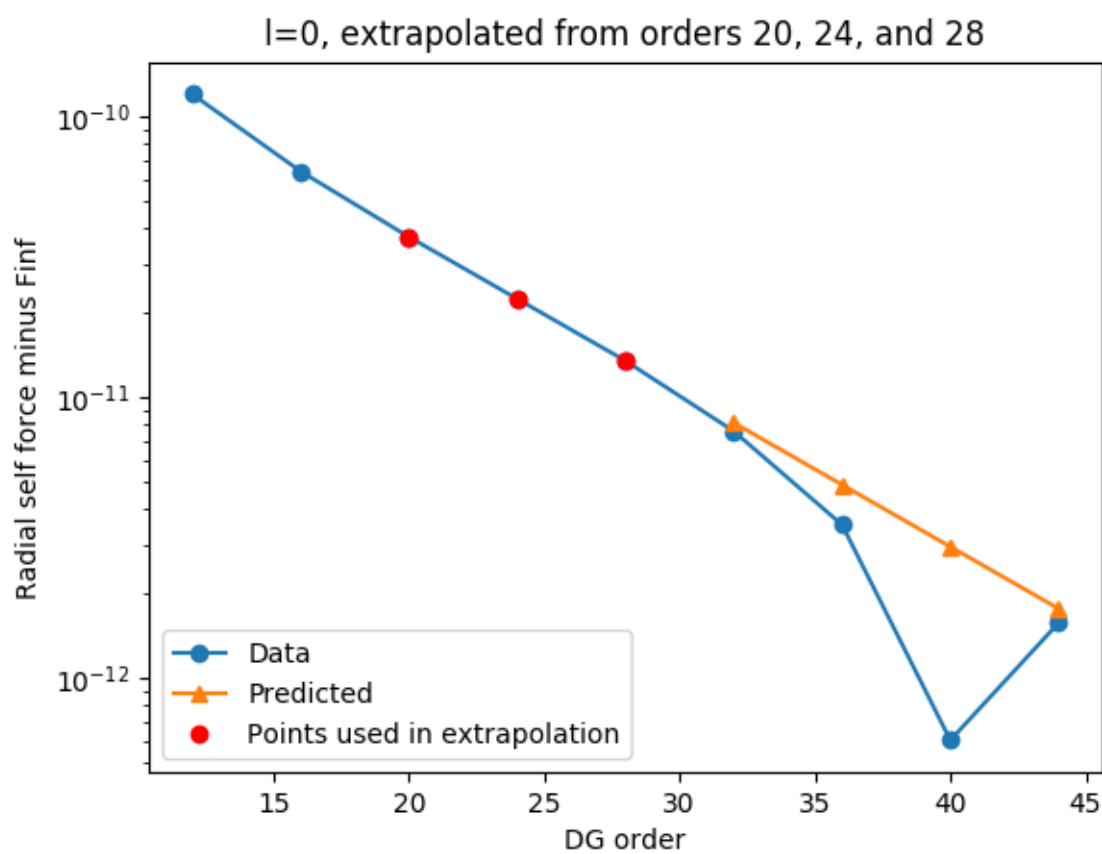


Figure 6.9:  $l=0$  mode with line-segment fit-chosen starting order produces convergence plot with long exponentially converging region

# Chapter 7

## Extrapolating the mode-summed self-force to include contributions from an infinite number of spherical harmonic modes

INCLUDE CITATION AND FUNCTIONAL FORM, FUNCTIONAL FORM OF MODE SUM

$$F_r(l) = \frac{a}{(2l-1)(2l+3)} + \frac{b}{(2l-3)(2l-1)(2l+3)(2l+5)} \\ + \frac{c}{(2l-5)(2l-3)(2l-1)(2l+3)(2l+5)(2l+7)} + \dots \quad (7.1)$$

$$\sum_n^{\infty} F_r(l) = \frac{an}{4n^2-1} + \frac{bn}{3(9-40n^2+16n^4)} \\ + \frac{cn}{5(2n-5)(2n-3)(2n-1)(2n+1)(2n+3)(2n+5)} + \dots \quad (7.2)$$

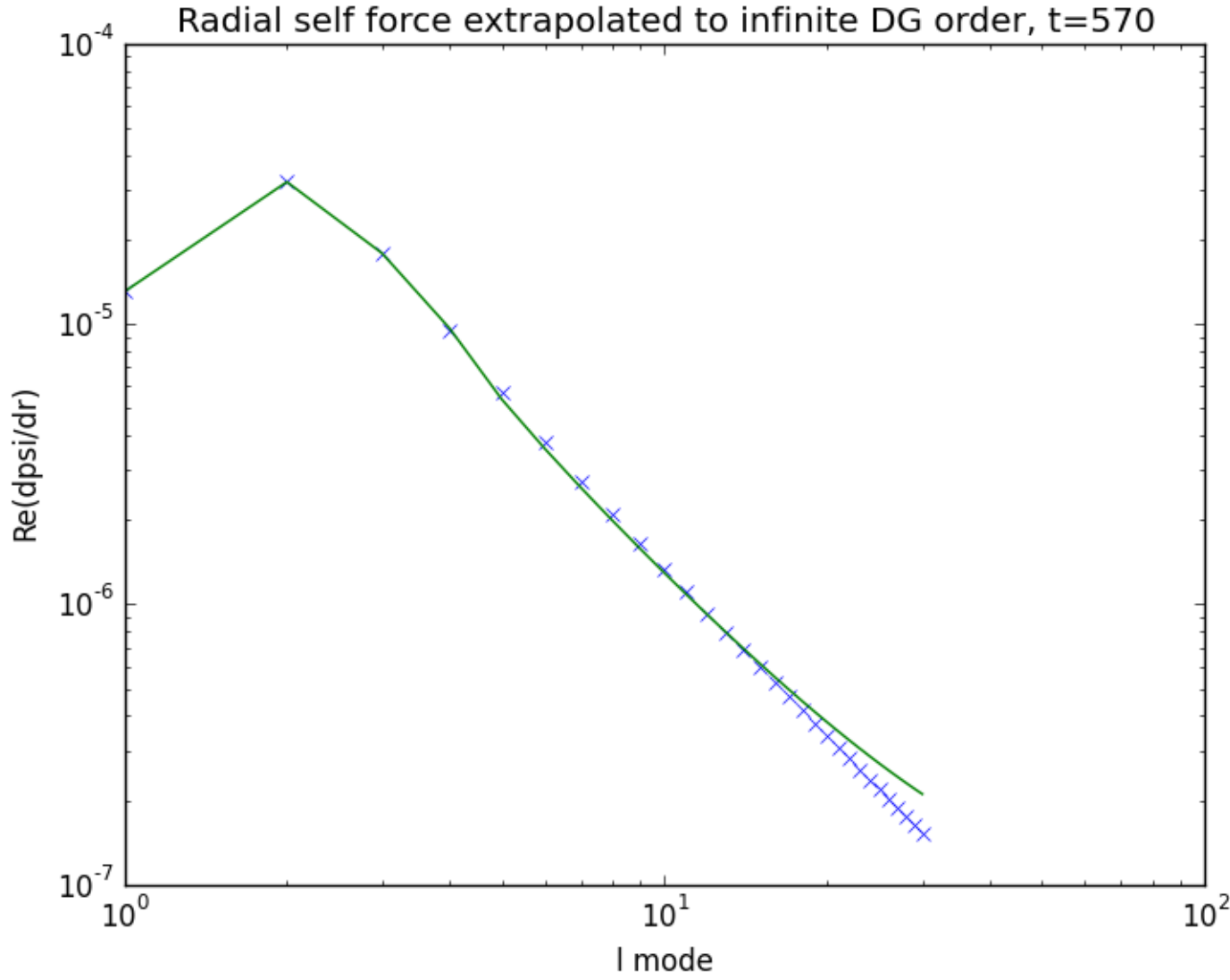


Figure 7.1: Three term fit of  $l$ -mode vs  $F_{\text{inf}}$ . Note how the fit is bad at high  $l$ . There are an infinite number of additional terms that can be added to the fit to account for this deviation. However, it is also fundamentally difficult to fit an exponentially converging function. See Chapter 8.1.

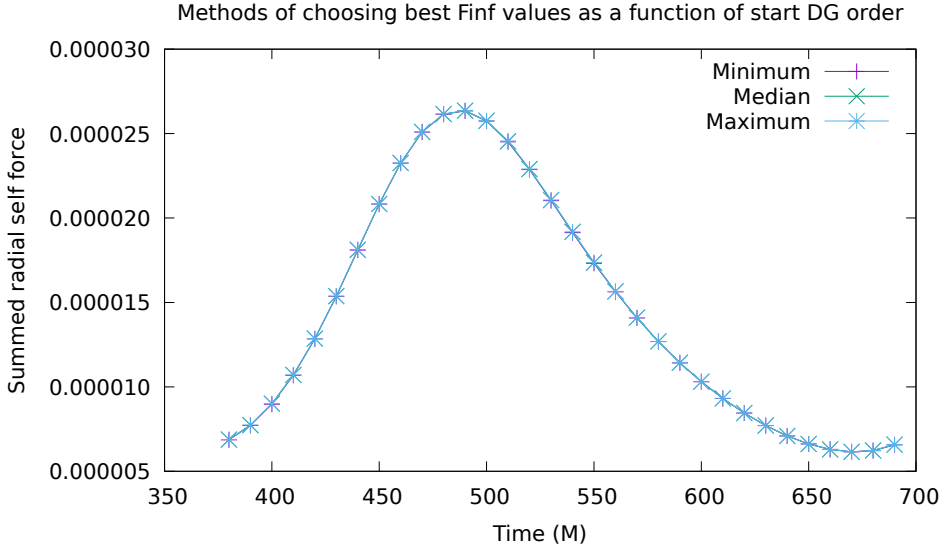


Figure 7.2: This is the actual summed, doubly extrapolated, radial self force, measured in three different ways as described in the three figures above.

take standard deviation of surface plot as well as average.

### 7.0.1 Fractional errors

### 7.0.2 Structure of the error compared to the evolution in time



Total radial self force, using DG error extrapolation per l-mode, t=635

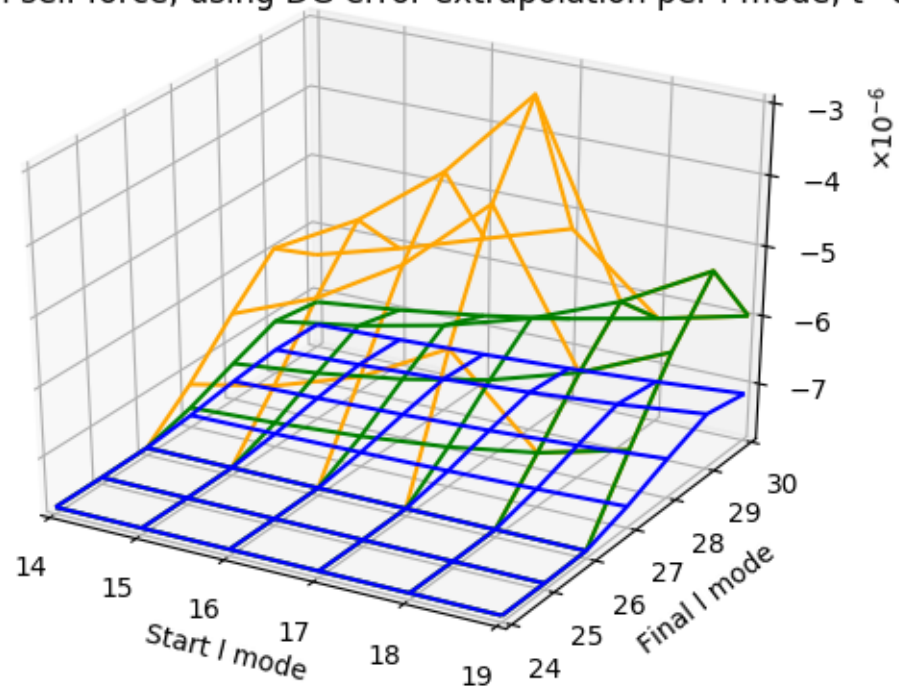


Figure 7.3: t=635, 2, 3, and 4 term fits over a broad range of lmin and lmax values. Note the roundoff noise at high lmax. Aphelion, where this effect is worst.

Total radial self force, using DG error extrapolation per l-mode,  $t=635$

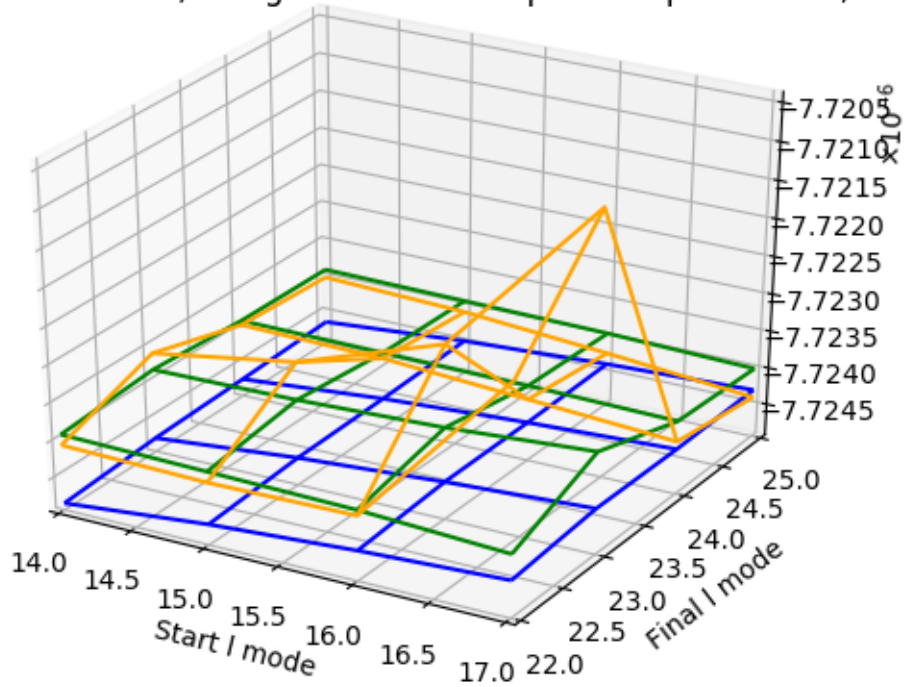


Figure 7.4:  $t=635$ , 2, 3, and 4 term fits over a small range of  $l_{\min}$  and  $l_{\max}$ . This is the actual range used to estimate the total self force. Aphelion, where the roundoff noise is worst. Note that there is not a large difference between two and three terms, and that four terms is less smooth a surface, suggesting that it is more subject to round off noise. Three terms is preferred.

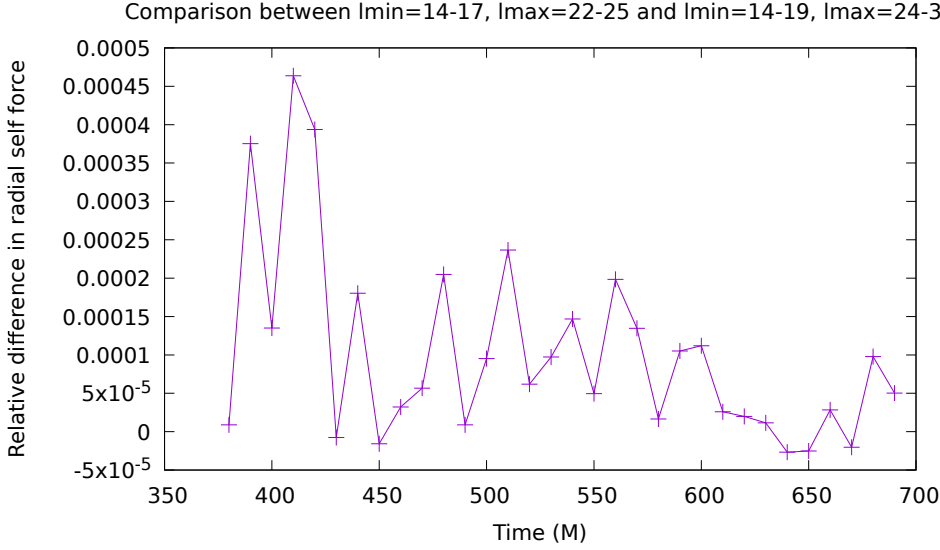


Figure 7.5: This is the relative difference between the total radial self force measured in two different ways. In both cases, the self force was extrapolated to infinite order at every  $l$ -mode at every possible DG starting order. The infinite DG order self forces over the various starting orders were sorted, eliminating NaNs. The median was chosen for each  $l$ -mode. Then the self force as a function of  $l$ -mode was fit to its three term form, and the sum was summed from zero to  $l_{\max}$ , then extrapolated from  $l_{\max} + 1$  to infinity using an analytic form determined using Mathematica. All possible choices with  $l_{\min}$  between 14 and 17 and  $l_{\max}$  between 22 and 25 were averaged to obtain the total radial self force as a function of time. Similarly, all possible choices with  $l_{\min}$  between 14 and 19 and  $l_{\max}$  between 24 and 30 were averaged to obtain the total radial self force as a function of time. This plot shows the relative difference. I believe the smaller range is in the denominator.

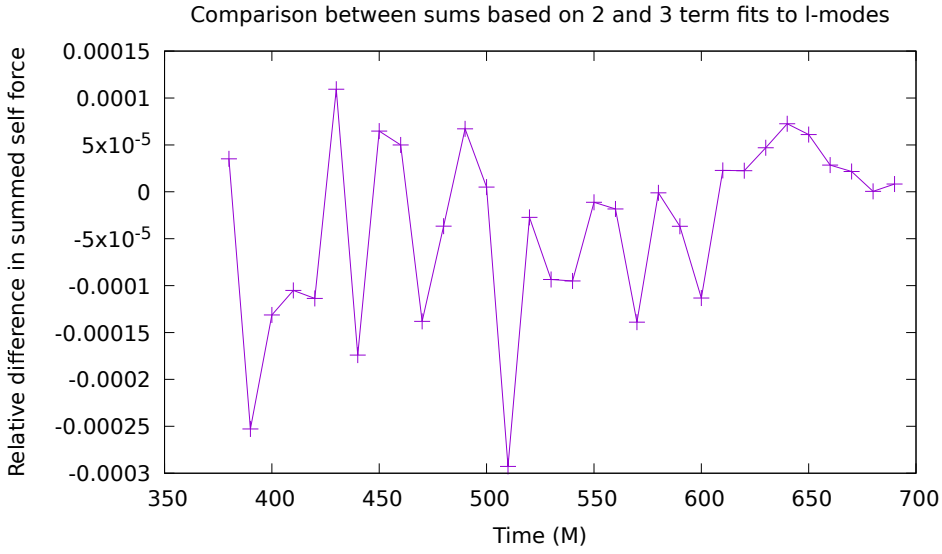


Figure 7.6: This figure was produced in the same manner as the previous figure, averaging over the smaller range, only it is a comparison between including either two or three terms in the l-mode fit. I believe the three term fit is in the denominator of the relative difference.

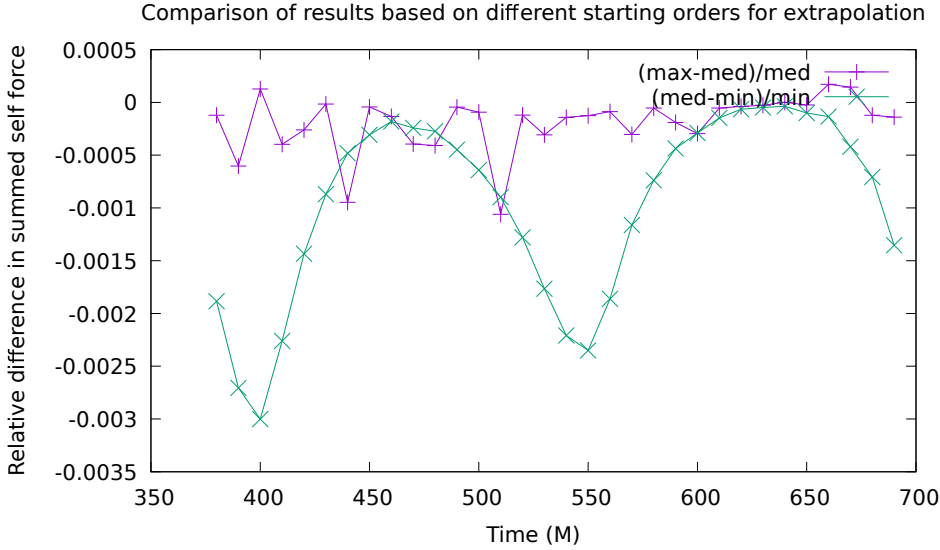


Figure 7.7: This figure was produced in a similar manner to the first figure, only instead of using the median, it is a comparison between using the median, the maximum, and the minimum. The purple line is the relative difference between the maximum and the median, which is subject to roundoff error due to the potential for the maximum to contain roundoff error. The green line is the relative difference between the median and the minimum, which is subject to effects due to failure to converge. I suspect the median is the best compromise between these two effects, rejecting outliers in both directions, though it is a simplistic approach to doing so, and does not guarantee success. It is possible to have a starting order that has not converged and is also in the roundoff regime, for example. A better guarantee of success, though not a certain one, would be to do a fit over part of the error convergence plot to determine exponentiality, by fitting a line in semilog scale. However, this seems unnecessarily complex at this time.

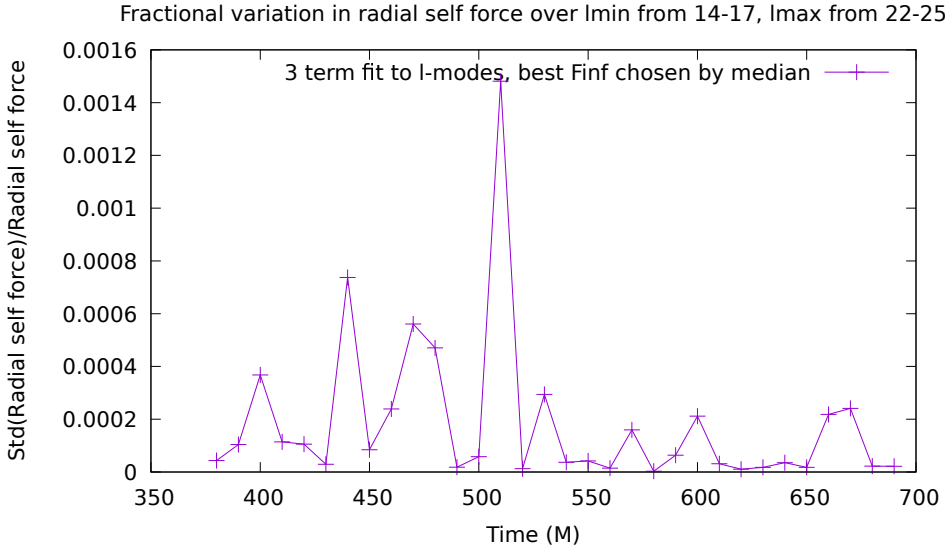


Figure 7.8: 3 term, median method

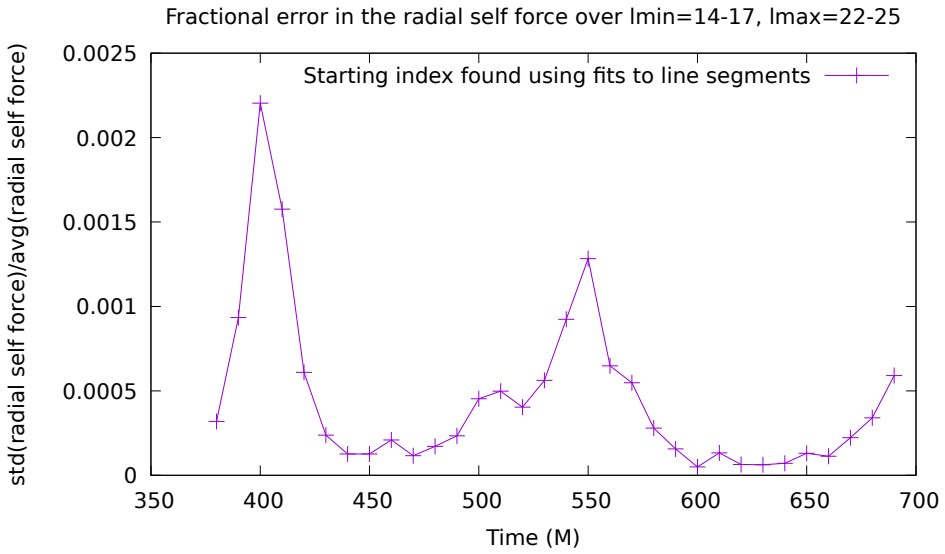


Figure 7.9: 3 term, fit method

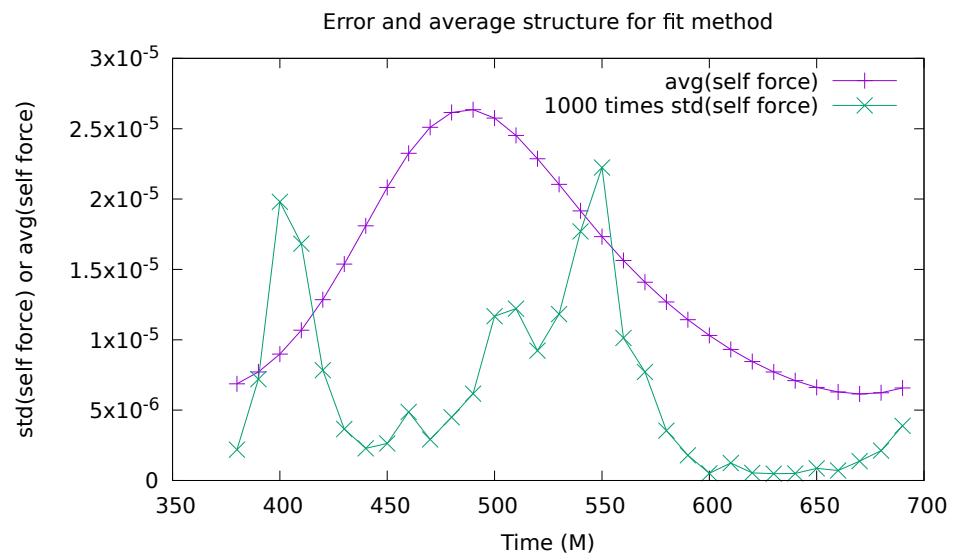


Figure 7.10: The structure of the absolute error in comparison to the evolution in time for the fit method

# Chapter 8

## Improving mode fits via a power law scaled weight factor in $\chi^2$ sum

### 8.0.1 Relative error as a function of mode

We can understand why it is so hard to produce good fits by examining the relative error between different fitting techniques as a function of mode. Look at the relative error between the fit method and the median method. One would hope that absolute error decreases with  $l$ , such that the infinite series would be convergent. Since the self force over  $l$  scales as a power law that goes as  $l^{-2}$  to the first order, I suggest a weight that scales as  $l^{-2}$ . A weighted fit is of the form

$$\chi^2 = \sum \frac{(f(x_i) - y_i)^2}{\sigma_i} \quad (8.1)$$

where  $\sigma_i$  is a weight related to the “error” or “uncertainty”, in this case the truncation or roundoff error depending which regime the mode is in. Absolute values of weights don’t matter unless the reduced  $\chi^2$  is used to select the best fit.

Absolute error increases as  $l$ .

### 8.1 TODO

He also wants convergence plots of the fit data versus the median data for some bad times. I also want a plot that shows the raw data before the subtraction of the offset for some time. Modify code to use saved raw data.



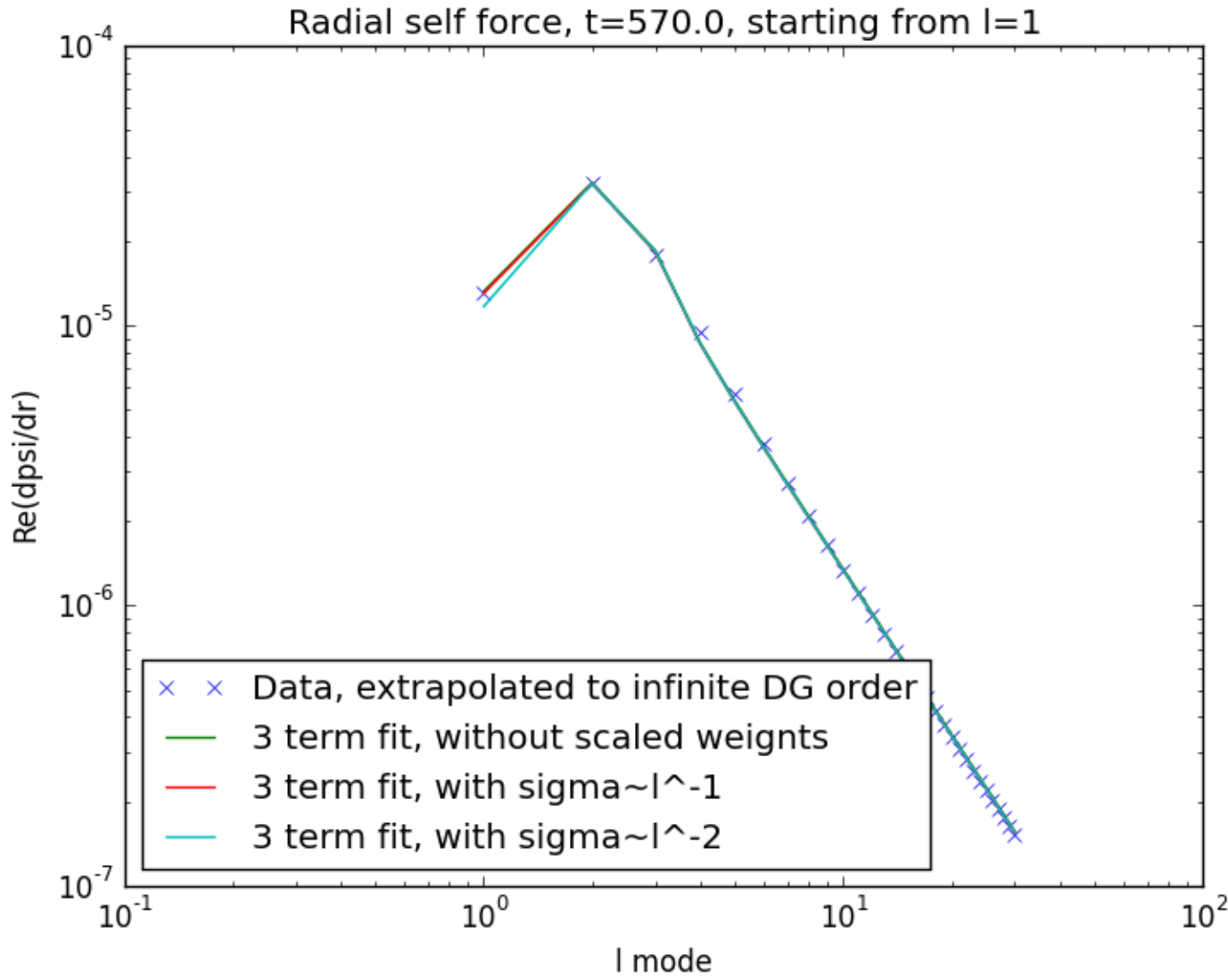


Figure 8.1:  $t=570$ ,  $l=1$ , three term fit with two different power law scales for weights in comparison to unscaled weights ( $\sigma = 1$ ).

## Variation of total radial self force with start and end points of fit

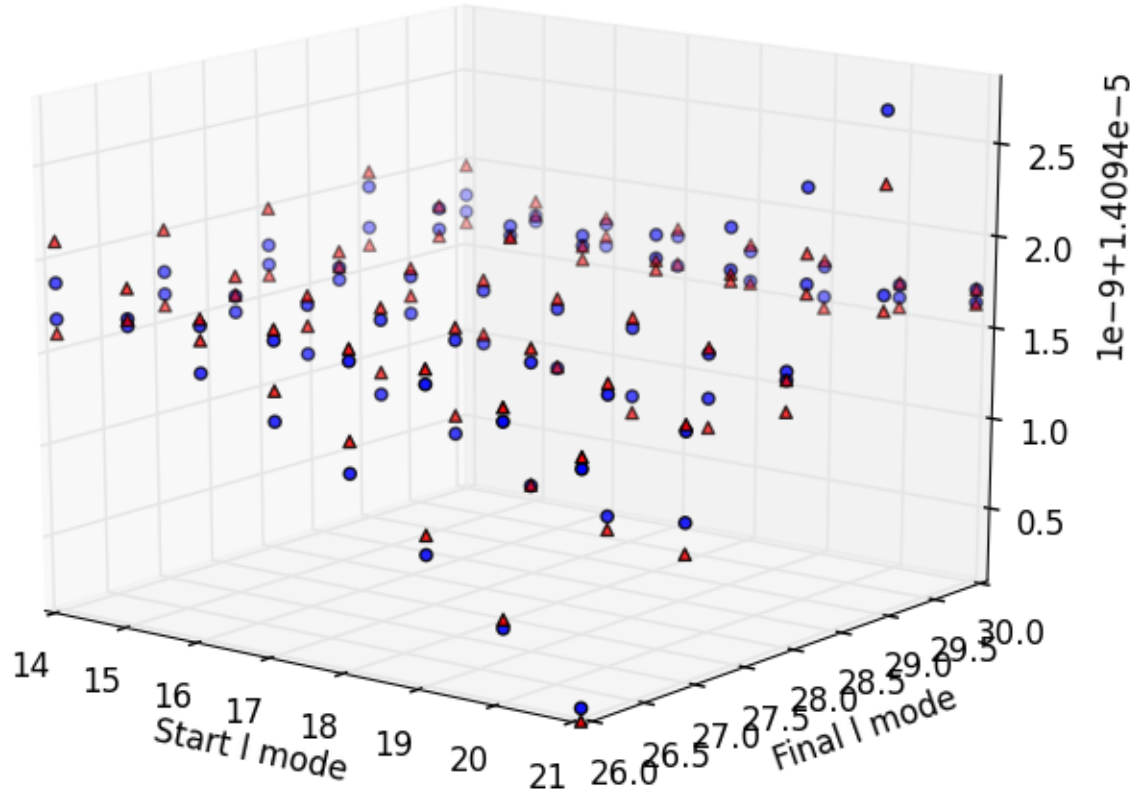


Figure 8.2: The difference between the triangles and the circles shows that the difference in the total radial self force between the presence of a  $\sigma \sim l^{-2}$  weight and no weight is unimportant compared to the difference in the total radial self force between various start and end points of the l-mode fit.

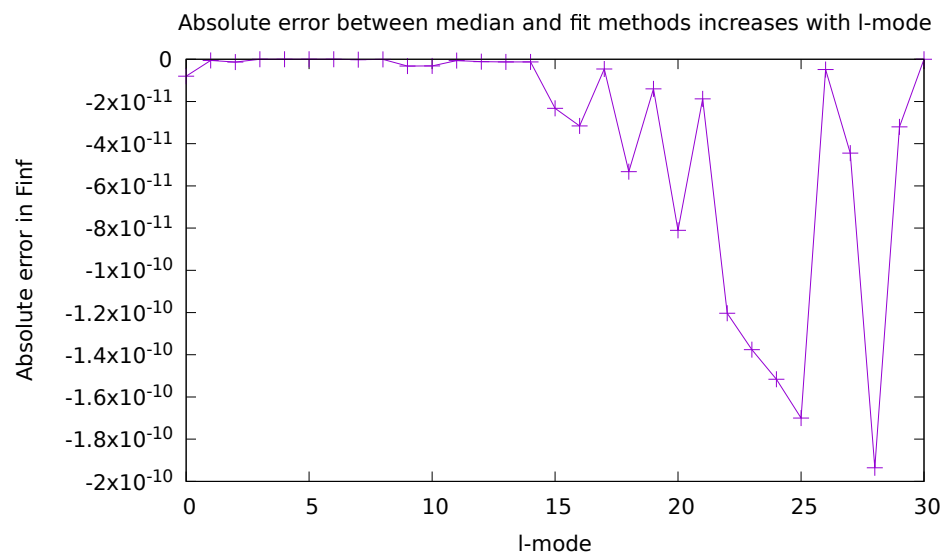


Figure 8.3: Absolute error between fit and median techniques increases with l-mode, explaining why the difference between weight and no weight fit techniques is unimportant.

# Chapter 9

## Future work: generic orbits via the osculating orbits framework

### 9.1 plans for the future

going to test Peter Diener's generic orbits and help him develop them further.

#### 9.1.1 methods

effective source osculating orbits time dependent coordinate transformation world tube already implemented with accelerated orbits though I have not run these. future work: make self consistent evolution work.

# References

- [1] Miller, Jeremy; Wardell, Barry; Pound, Adam. (2016). Second-order perturbation theory: the problem of infinite mode coupling. *arXiv:1608.0783v1*.
- [2] Heffernan, Anna. (2012). The Self-Force Problem: Local Behavior of the Detweiler-Witing Singular Field. University College Dublin. *arXiv:1403.6177v1*.
- [3] Yang, Huan; Zimmerman, Aaron; Zenginoglu, Anil; Zhang, Fan; Berti, Emanuele; Chen, Yanbei. (2013). Quasinormal modes of nearly extremal Kerr spacetimes: spectrum bifurcation and power-law ringdown. *arXiv:1307.8086v1*.
- [4] Berti, Emanuele; Cardoso, Vitor; Starinets, Andrei O. Quasinormal modes of black holes and black branes. *arXiv:0905.2975v2*
- [5] Philipp, Dennis; Perlick, Volker. (2015). On analytic solutions of wave equations in regular coordinate systems on Schwarzschild background. *arXiv:1503.08101v1*
- [6] Diaz-Rivera, Luz Maria; Messaritaki, Eirini; Whiting, Bernard F.; Detweiler, Steven. (2004). Scalar field self-force effects on orbits about a Schwarzschild black hole. *arXiv:gr-qc/0410011v1*.
- [7] Diener, Peter; Vega, Ian; Wardell, Barry; Detweiler, Steven. Self-consistent orbital evolution of a particle around a Schwarzschild black hole. *arXiv:1112.4821v3*.
- [8] Dirac, P. A. M. (1938). Classical theory of radiating electrons. *Royal Society Publishing*.
- [9] Amaro-Seoane, Pau; Gair, Jonathon R.; Pound, Adam; Hughes, Scott A.; Sopuerta, Carlos F. (2014). Research Update on Extreme-Mass-Ratio Inspirals. *arXiv:1410.0958v1*.
- [10] Gair, Jonathan R.; Porter, Edward K. (2012). Observing extreme-mass-ratio inspirals with eLISA/NGO. *arXiv:1210.8066v1*
- [11] Gralla, Samuel E.; Harte, Abraham I.; Wald, Robert M. (2009). A Rigorous Derivation of Electromagnetic Self-force. *arXiv:0905.2391v2*.
- [12] Heffernan, Anna; Ottewil, Adrian; Wardell, Barry; (2013). High-order expansions of the Detweiler-Whiting singular field in Schwarzschild spacetime. *arXiv:1204.0794v4*.
- [13] Bernuzzi, Sebastiano; Nagar, Alessandro; Zenginoglu, Anil. (2011). Binary black hole coalescence in the large-mass-ratio limit: the hyperboloidal layer method and waveforms at null infinity. *arXiv:1107.5402v2*.
- [14] Danzmann, Karsten. (2017). LISA Laser Interferometer Space Antenna: A proposal in response to the ESA call for L3 mission concepts.
- [15] Babak, Stanislav. (2017). Science with the space-based interferometer LISA. V: Extreme mass-ratio inspirals. *arXiv:1703.09722v1*.

- [16] Miller, Jeremy; Wardell, Barry; Pound, Adam. (2016). Second-order perturbation theory: the problem of infinite mode coupling. *arXiv:1608.06783v1*.
- [17] Mino, Yasushi; Sasaki, Misao; Tanaka, Takahiro. (1996). Gravitational Radiation Reaction to a Particle Motion. *arXiv:gr-qc/9606018v1*.
- [18] Yunes, Nicolas; Wofgang, Tichy; Owen, Benjamin J.; Brüggmann, Bernd. (2006). Binary black hole initial data from matched asymptotic expansions. *arXiv:gr-qc/0503011v3*.
- [19] Poisson, Eric; Pound, Adam; Vega, Ian. (2011). The Motion of Point Particles in Curved Spacetime. *arXiv:1102.0529v3*.
- [20] Pound, Adam. (2012). Second-order gravitational self-force. *arXiv:1201.5089v2*.
- [21] Pound, Adam. (2017). Nonlinear gravitational self-force: second-order equation of motion. *arXiv:1703.02836v1*.
- [22] Pound, Adam; Poisson, Eric. (2008). Osculating orbits in Schwarzschild spacetime, with an application to extreme mass-ratio inspirals. *Phys. Rev. D* 77, 044013.
- [23] Quinn, Theodore, C. (2000). Axiomatic approach to radiation reaction of scalar point particles in curved spacetime. *arXiv:gr-qc/0005030v1*.
- [24] Quinn, Theodore C.; Wald, Robert M. An Axiomatic approach to electromagnetic and gravitational radiation reaction of particles in curved spacetime. *arXiv:gr-qc/9610053v1*.
- [25] Field, Scott E.; Hesthaven, Jan S.; Lau, Stephen R. Discontinuous Galerkin method for computing gravitational waveforms from extreme mass ratio binaries. *arXiv:0902.1287v2*.
- [26] Zenginoglu, Anil; Khanna, Gaurav. (2011). Null infinity waveforms from extreme-mass-ratio inspirals in Kerr spacetime. *arXiv:1108.1816v2*.
- [27] Vega, Ian; Diener, Peter; Tichy, Wolfgang; Detweiler, Steven. (2009). Self-force with (3+1) codes: a primer for numerical relativists. *arXiv:0908.2138v1*.
- [28] Vega, Ian; Wardell, Barry; Diener, Peter. (2011). Effective source approach to self-force calculations. *arXiv:1101.2925v1*.
- [29] Vega, Ian; Wardell, Barry; Diener, Peter; Cupp, Samuel; Haas, Roland. (2013). Scalar self-force for eccentric orbits around a Schwarzschild black hole. *arXiv:1307.3476v2*.
- [30] Vega, Ian; Wardell, Barry; Diener, Peter; Cupp, Samuel; Hass, Roland. (2013). Scalar self-force for eccentric orbits around a Schwarzschild black hole. *arXiv:1307.3476v2*.
- [31] Wardell, Barry. (2015). Self-Force: Computational Strategies. *arXiv:1501.07322v3*.

- [32] Wardell, Barry; Vega, Ian; Thornburg, Jonathan; Diener, Peter. (2012). Generic effective source for scalar self-force calculations. *arXiv:1112.6355v3*.
- [33] LIGO Virgo Collaboration. (2016). Observation of Gravitational Waves from a Binary Black Hole Merger. *Phys. Rev. Lett.* 116, 061102.
- [34] LIGO Virgo Collaboration. (2016). GW151226: Observation of Gravitational Waves from a 22-Solar-Mass Binary Black Hole Coalescence. *Phys. Rev. Lett.* 116, 241103.
- [35] LIGO Virgo Collaboration. (2017). GW120104: Observation of a 50-Solar-Mass Binary Black Hole Coalescence at Redshift 0.2. *Phys. Rev. Lett.* 118, 221101.
- [36] LIGO Virgo Collaboration. (2016). Observing Gravitational-wave Transient GW150914 with Minimal Assumptions. *Phys. Rev. D* 93, 122004.
- [37] LIGO Virgo Collaboration. (2016). GW150914: First Results from the Search for Binary Black Hole Coalescence with Advanced LIGO. *Phys. Rev. D* 93, 122003.
- [38] LIGO Virgo Collaboration. (2016). The Rate of Binary Black Hole Mergers Inferred from Advanced LIGO Observations Surrounding GW150914. *Accepted Astrophys. J. Lett*
- [39] LIGO Virgo Collaboration. (2016). Astrophysical Implications of the Binary Black-Hole Merger GW150914. *Astrophys. J. Lett* 818, L22.
- [40] LIGO Virgo Collaboration. (2016). Tests of General Relativity with GW150914. *Phys. Rev. Lett.* 116, 221101.
- [41] LIGO Virgo Collaboration. (2016). GW150914: Implications for the Stochastic Gravitational Wave Background from Binary Black Holes. *Phys. Rev. Lett.* 116, 131102.
- [42] LIGO Virgo Collaboration. (2016). Calibration of the Advanced LIGO Detectors for the Discovery of the Binary Black-hole Merger GW150914. *Submitted to Phys. Rev. D*.
- [43] LIGO Virgo Collaboration. (2016). Characterization of Transient Noise in Advanced LIGO Relevant to Gravitational Wave Signal GW150914. *Class. Quant. Grav.* 33, 134001.
- [44] LIGO Virgo Collaboration and ANTARES and IceCube Collaborations. (2016). High-energy Neutrino Follow-up Search of Gravitational Wave Event GW150914 with ANTARES and IceCube. *Phys. Rev. D* 93 122010.
- [45] LIGO Virgo Collaboration. (2016). GW150914: The Advanced LIGO Detectors in the Era of First Discoveries. *Phys. Rev. Lett.* 116, 131103.
- [46] LIGO Virgo, ASKAP, BOOTES, Dark Energy Survey and Camera, GW-EM, Fermi GBM and LAT, GRAWITA, INTEGRAL, IPTF, InterPlanetary, J-GEM, La Silla-Quest, Liverpool Telescope, LOFAR, MASTER, MAXI, MWA, PAN-STARRS,

- PESSTO, PI of the Sky, SkyMapper, Swift, TAROT, Zadko, Algerian National Observatory, C2PU, TOROS, and VISTA Collaborations. (2016). Localization and Broadband Follow-up of the Gravitational-wave Transient GW150914. *Astrophys. J. Lett.* 826, L13.
- [47] Bambi, Cosimo. (2017) Testing black hole candidates with electromagnetic radiation. *Reviews of Modern Physics* 89.
  - [48] Martynov, D.V., et al. (2016). Sensitivity of the Advanced LIGO detectors at the beginning of gravitational wave astronomy. *Phys. Rev. D* 93, 112004.
  - [49] Poisson, Eric; Pound, Adam; Vega, Ian. (2011). The motion of point particles in curved spacetime. *Living Reviews in Relativity.* 14, 7.
  - [50] Hesthaven, Jan S.; Warburton, Tim. (2008). *Nodal Discontinuous Galerkin Methods: Algorithms, Analysis, and Applications*. Springer.
  - [51] Saulson, Peter R. (1994). *Fundamentals of Interferometric Gravitational Wave Detectors*. World Scientific Publishing Co.
  - [52] Press, William H.; Teukolsky, Saul A.; Vetterling, William T.; Flannery, Brian P. (2002). *Numerical Recipes in C++: The Art of Scientific Computing*. The Press Syndicate of the University of Cambridge.
  - [53] Wolfram, Stephen. (2016). *An Elementary Introduction to the Wolfram Language*. Wolfram-Media, inc.
  - [54] Newman, Mark. (2013). *Computational Physics*. University of Michigan.
  - [55] Wald, Robert M. (1984). *General Relativity*. The University of Chicago.
  - [56] Carroll, Sean M. (2004). *An Introduction to General Relativity Spacetime and Geometry*. Addison Wesley.
  - [57] Misner, Charles W.; Thorne, Kip S.; Wheeler, John Archibald. (1973). *Gravitation*. W. H. Freeman and Company.



# Vita

My past research has been on comet photometry, x-ray bursts, gravitational lensing and cosmology, exoplanets, neutrino oscillations, theoretical particle physics, gravitational waves, and gravity gradient noise. Most of my background is in simulation, whether statistical or theoretical. I think of myself as a computational physicist and a multimessenger astronomer, though I am not sure that term is widely used. What I mean by it is that I have a broad background in particle physics, particle astrophysics, gravitational wave astronomy, and traditional astronomy. If we can consider my various meanderings as one path toward these two goals, I have been walking this path for more than a decade.

Now I am a fourth year graduate student at Louisiana State University, exactly where I intended to be. My coworkers are good friends. I got to perform photometry of exoplanets with a telescope and analyze the data for myself, bringing a previous project full circle. I have worked on LIGO during the time of three detections. I have had the opportunity to begin to learn multiple techniques for speeding up code and measuring that speed up on supercomputers. I have done a little work with databases and more with numerical algorithms, and learned a couple of new programming languages. I have had the opportunity to continue to contribute to the field of general relativity and participate in a department where my broad background in the connections between various fields of astronomy is valued. I have helped supervise undergraduate research progress and made a lesson plan for and taught a graduate class, once. This document contains the research I have produced in the last three years since I arrived on June 3, 2014 at LSU and began working with Peter Diener. These have been the best three years of my life.

When interpreting the name on this document, please understand that I am female to male transgendered and that my legal name is Susan Elaine Dorsher but that I go by Steven James Dorsher.